https://doi.org/10.5194/wes-2026-89
Preprint. Discussion started: 3 June 2026

Open Access
WIND
ENERGY
SCIENCE
DISCUSSIONS

IEA Wind Task 46 Aerodynamic Benchmark: Computational Aerodynamics Approaches for Assessing Blade Airfoil Performance Reduction due to Leading Edge Degradation

M. Sergio Campobasso[a], Alessio Castorrini[b,a], David Bretos[c], Beatriz Mendez[c], David C. Maniaci[d], Johannes N. Theron[e], Alexander Meyer Forsting[f], Niels N. Sørensen[f], Kisorthman Vimalakanthan[g], Marco Caboni[g], Ruben Gutierrez[h], Yana Gorbachova[h], Aya Aihara[i], and Francesco Grasso[j]

[a]School of Engineering, Lancaster University, Lancaster, United Kingdom
[b]Department of Mechanical and Aerospace Engineering, Sapienza University of Rome, Rome, Italy
[c]National Renewable Energy Center (CENER), Sarriguren, Spain
[d]Sandia National Laboratories, Albuquerque, New Mexico, United States
[e]Fraunhofer IWES, Oldenburg, Germany
[f]DTU Wind, Technical University of Denmark, Risø, Denmark
[g]TNO, Wind Energy Technology, Petten, The Netherlands
[h]Nordex SE, Langenhorner Chaussee 600, 22419 Hamburg, Germany
[i]National Institute of Advanced Industrial Science and Technology (AIST), Fukushima, Japan
[j]Vestas Technology Centre Porto, Leça do Balio, Porto, Portugal

Correspondence: M. Sergio Campobasso (m.s.campobasso@lancaster.ac.uk)

Abstract. Leading edge (LE) surface degradation of wind turbine (WT) blades caused by insect accumulation, erosion and other environmental agents reduces the aerodynamic performance of the blades, causing WT power and energy yield losses. Estimating these losses is paramount for cost-informed maintenance planning. Computational Fluid Dynamics (CFD) can predict aerodynamic performance losses. However, sensitivity of these predictions to physical model choice and detailed model settings can be large. To assess this sensitivity, the International Energy Agency Task 46 – Erosion of Wind Turbine Blades, developed the First Aerodynamic Benchmark, presented herein. The performance degradation of the NACA 63_3-418 airfoil due to moderate and severe LE degradation, assessed experimentally in two wind tunnel measurement campaigns, is studied. The clean and degraded airfoil performance predicted by seven CFD codes and two low-fidelity methods are cross-compared and benchmarked against measurements. A utility-scale WT featuring the NACA 63_3-418 airfoil on the outboard blade is used to determine the resulting power and energy losses onshore and offshore. Most codes succeed in predicting the measured airfoil performance reduction due to moderate LE degradation before stall. Consequently, all energy loss estimates are close. Conversely, the variability of the predicted aerodynamic performance reduction due to severe LE degradation is larger, and the variability of the resulting energy losses is also larger than at moderate LE degradation. These results underline both the significant sensitivity to the specific analysis set-up and the need for further research into methods for predicting the impact of advanced LE degradation, such as geometry perturbation-resolving simulations.

1 Introduction

Wind energy is contributing substantially to the decarbonization of electricity generation worldwide. The exploitation of offshore wind is on the rise and is projected to increase even more rapidly in the near future, but outstanding and anticipated future technological and economic challenges in the offshore operation and maintenance (O&M) of new wind turbines (WTs) will be exacerbated by the large size of these machines, the need for new suitable infrastructure, and the increasing load severity associated with the ongoing climate change. Leading edge (LE) surface degradation of WT blades is one of the critical challenges that affect both offshore and onshore installations. This is because LE degradation increases surface roughness, an occurrence resulting in reductions of the lift force and increase of the drag force on the blade sections. These phenomena reduce rotor torque and WT power, and, ultimately, the WT Annual Energy Production (AEP). Therefore, often unplanned costly remedial maintenance is required to restore a LE state adequate to energy efficient operation of the WT.

Following the taxonomy proposed by Wood and Lu (2021), the environment-driven mechanisms yielding LE geometry alterations may be subdivided into additive and subtractive processes. An example of temporary LE geometry degradation caused by an additive process is blade icing, which may occur in cold climates. WT blade icing causes AEP losses that often exceed 5% (Barber et al., 2011; Jin et al., 2021). This loss is caused by the decreased aerodynamic performance resulting from both the LE shape variation due to ice layers and the roughness of the surface of the ice layers. The study of Caccia and Guardone (2023) reported the strong influence of the surface roughness of the ice deposits in the WT power loss. Other forms of additive processes, such as surface fouling due to insect accumulation, also affect aerodynamic performance. For example, the study by Ehrmann et al. (2017) reported that the increased LE roughness resulting from this kind of surface degradation can reduce the power of a 5 MW WT by 1 to 2%.

Over long periods of time, continuous exposure of WT blades to sand (Guan et al., 2025; Wang et al., 2024), rain Keegan et al. (2013), hail (Keegan et al., 2013; Pryor and Barthelmie, 2026) and other airborne particles leads to LE erosion (LEE), resulting in both AEP losses, due to blade performance degradation, and the need for more complex and costly O&M (Herring et al., 2019; Mishnaevsky et al., 2021). LEE, the result of subtractive processes, manifests itself with an increase of the surface roughness at initial and intermediate stages, with roughness heights smaller than the boundary layer (BL) height, whereas it yields noticeable LE geometry alterations with size comparable to the total thickness of the LE structure at severe damage stages Han et al. (2018); Im and Kim. (2019); Cappugi et al. (2021); Campobasso et al. (2023). Thus, at advanced LEE stages, the blade performance degradation is caused by both the large perturbations of the LE geometry, due to the removal of the LE protective layer and portions of the composite substrate, and the roughness of the exposed composite substrate itself. Similarly to the case of icing, numerical studies have shown that the detrimental impact of surface roughness and larger geometry alteration on WT power may be comparable in magnitude (Ortolani et al., 2022; Castorrini et al., 2023).

The discussion above highlights that the prediction of WT power and AEP reductions due to LE degradation, which is critical to maintenance planning (Lopez et al., 2024) and evaluating new active LE protection technologies (Bech et al., 2018; Campobasso et al., 2026) requires estimating the reduction of WT blade aerodynamic performance due to surface roughness. This is a general requirement fairly independent of the root cause of the surface degradation and, to a certain extent, also independent of the severity of the LE degradation. The latter observation is motivated by the fact that the detrimental impact of severe LE degradation can be analyzed using a scale separation approach (Ortolani et al., 2022; Caccia and Guardone, 2023), whereby the effects of relatively small surface roughness can be modeled with a semi-empirical approach, such as the equivalent sand-grain roughness method (Nikuradse, 1950; Schlichting, 1937) embedded in general-purpose analysis software (Koodly Ravishankara et al., 2021), and the impact of large perturbations can be analyzed by resolving the geometry perturbation (Han et al., 2018; Campobasso et al., 2022).

For specific WT airfoils, the performance degradation due to LE roughness can be determined experimentally, using wind tunnel testing (Timmer and Schaffarczyk, 2004; Somers, D.M., 2004; Kruse et al., 2021). Wind tunnel testing is pivotal for validating computational aerodynamics codes used in industrial applications and academic research, since these codes are the only means to analyze the performance of airfoils and/or operating conditions for which no experimental data are available. It is therefore paramount to the wind energy sector to have access to comprehensive databases of validation studies, including the assessment of the predictive capabilities of WT airfoils with clean and roughened LE using state-of-art methods adopted in present industrial and academic practice. This requirement prompted the development of the First Aerodynamic Benchmark of "Task 46 – Erosion of Wind Turbine Blades" (IEA Wind TCP), a Technology Collaboration Programme (TCP) of the International Energy Agency (IEA). The main focus of the benchmark is the prediction of the aerodynamic performance degradation of WT airfoils due to different levels of LE roughness. In line with this, this article focuses on the aerodynamic performance of a WT airfoil without and with LE roughness, and reports and discusses the analyses of eight participants from academia and industry, namely Lancaster University (LU), Technical University of Denmark (DTU), National Renewable Energy Centre of Spain (CENER), wind turbine manufacturer NORDEX, the National Institute of Advanced Industrial Science and Technology of Japan (AIST), the Netherlands Organization for Applied Scientific Research (TNO), Fraunhofer Institute for Wind Energy Systems (IWES) and wind turbine manufacturer VESTAS. Furthermore, the variability of the power and AEP losses of a utility-scale WT featuring the considered airfoil resulting from the variability of the airfoil performance determined by state-of-the-art wind tunnel measurements and the numerical predictions of all participants is also computed and thoroughly discussed.

The WT airfoil of the benchmark is the NACA 63_3-418 airfoil (Abbott and Von Doenhoff, 1959). A low and high level of LE roughness are considered. The measured performance data of two different wind tunnel campaigns are used to benchmark the computer-based assessments of the airfoil performance degradation due to the level of roughness considered. The utility-scale WT used to assess the impact of the considered LE degradation levels on power and AEP at typical onshore and offshore wind conditions is the National Renewable Energy Laboratory (NREL) 5 MW reference turbine (Jonkman et al., 2009).

The article is structured as follows. The airfoil test case and the wind tunnel experiments along with a brief description of the instrumentation and the available measured data are reported in Section 2. Section 3 lists the computational aerodynamics codes used by the all participants and describes the key methods used for modeling turbulence, laminar-to-turbulent BL transition and roughness effects by all adopted Computational Fluid Dynamics (CFD) codes. The general set-up of all CFD analyses is summarized in Section 4, with further detail for each CFD analysis provided in Appendix A. Section 5 is made up of three parts, with the first two reporting the main results of all aerodynamic analyses, and the third one presenting the comparative analysis of power and AEP losses based on the airfoil performance analyses of the first two parts. More specifically, Section 5.1 refers the low-level roughness; it cross compares all measured and computed airfoil performance assessments with clean and rough LE, and also cross-compares the roughness-induced variations of the lift coefficient c_l and the drag coefficient c_d estimated by measurements and simulations. Section 5.2 has a similar structure but it refers to the large roughness configuration. Section 5.3 cross compares power and AEP losses of the NREL 5 MW WT in onshore and offshore conditions using the measured and computed airfoil performance data for the two levels of LE roughness. A summary of the study and a brief discussion are provided in Section 6.

2 Test cases and wind tunnel measurements

The WT airfoil considered in the comparative analyses of this article is the 18% thick NACA 63_3-418 airfoil, well suited for the outboard blade portion of utility-scale WTs. The geometry of this airfoil is depicted in Fig. 1. The aerodynamic performance degradation caused by two levels of LE roughness is considered in this study. Two different wind tunnel measurement campaigns are considered to this aim. One, carried out in the wind tunnel of Texas A&M University, considers the performance degradation due to low-level LE roughness; the other, carried out in the wind tunnel of Delft University of Technology, focused on the case of large LE roughness. The performance of the clean airfoil was measured in both experiments. The experimental set-up adopted for the two wind tunnel measurement campaigns is briefly summarized in the next two subsections.

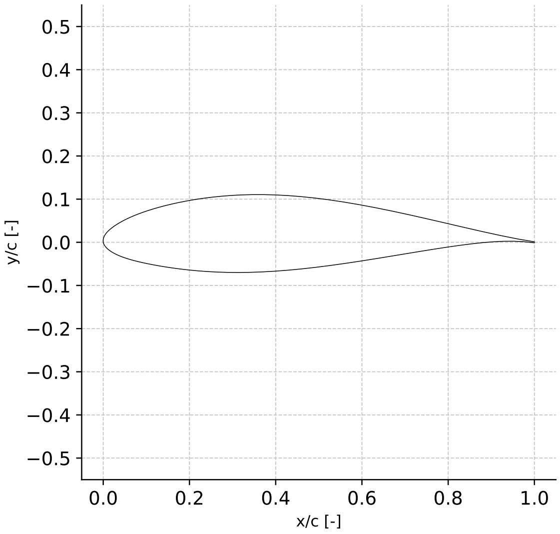

Figure 1. Geometry of NACA 63_3-418 airfoil.

2.1 Texas A&M wind tunnel measurement campaign

The first NACA 63_3-418 test case is part of a comprehensive experimental campaign carried out at the Oran W. Nicks low-speed wind tunnel at Texas A&M University (Ehrman, 2014; Maniaci et al., 2016). The turbulence intensity (TI) in the test section is about 0.25%. The airfoil model had chord c of 0.813 m and span length of 2.1 m, and was mounted vertically in the 2.1 m-high, 3.05 m-wide wind tunnel test section. To enable the study of various erosion configurations, the model was designed with a removable LE at 15% chord. Two piano hinges along the upper and lower main body of the model were used to securely attach the LE. Typical roughness patterns, including insect carcasses and LEE, were physically measured from operational wind turbine blades and used to generate statistically representative distributed roughness patterns which were realized using laser-cut adhesive vinyl sheets, allowing for parametric testing at different heights and surface-area-coverage densities (Ehrmann and White, 2014; Langel et al., 2015; Ehrman, 2014). Testing also included representation of measured paint chips using vinyl sheets and direct reproduction of an eroded LE using a 3D-printed LE insert. The complete dataset is available as an open archive (Maniaci and White, 2020).

Static pressure along the chord was measured by means of model pressure ports placed near midspan to reduce the effects of end wall flow near stall conditions; interference between ports was avoided by offsetting each pressure port by 9.5 mm in the spanwise direction. Lift force and pitching moment were calculated by integrating the surface pressure distribution. The drag force was calculated with a wake integral using the measurements of a wake rake placed placed at 0.9 chords downstream of the model trailing edge (TE). BL transition was measured using infrared thermography (IRT), which was verified through limited comparisons to hot wire anemometry measurements. IRT relies on the difference of heat transfer rate of turbulent and laminar boundary layers, with this parameter being higher for turbulent BLs due to their convective nature. A heating sheet was placed in the airfoil model. The higher heat transfer of turbulent BLs resulted in the model surface below the turbulent flow region being colder than below laminar flow regions, with IRT images detecting the sharp temperature variation and thus transition. An IRT image was acquired at each angle of attack (AoA) during each test run. Further information on the test rig and the measurement techniques is available in Ehrman (2014). It is noted that for the clean airfoil case, natural transition is triggered by Tollmien–Schlichting waves and transition occurs in a thin linear area parallel to the model LE. In the presence of LE roughness, however, as the AoA increases, natural transition is replaced by roughness-induced bypass transition. In this circumstance, the formation of turbulent wedges is observed and the transition front consists of a zigzagged line. A geometric criterion for selecting a single chordwise position to be used for comparison with 2D transitional flow simulations was proposed in Langel et al. (2017).

The Texas A&M test case considered in the analyses below consists of the clean airfoil and the roughened LE variant obtained by applying small adhesive disks of vinyl with elliptic shape to the LE. The roughness element height is K=200 μm, corresponding to a value of K=246 μm for a unitary chord. The roughness area density is 3%. The roughness elements are applied from the LE to 0.13c on the lower or pressure side (PS) and from the LE to 0.02c on the upper or suction side (SS). The Reynolds number Re based on the model chord is 3.2M.

2.2 Delft wind tunnel measurement campaign

The second NACA 63_3-418 test case is part of an experimental campaign carried out at the low-speed, low-turbulence wind tunnel of Delft University of Technology within the EU project Integrated Research Programme for Wind (IRPWIND) (Pires et al., 2018). The goals of the overall project were to test a standardized method for simulating and testing surface roughness aerodynamic effects at airfoil level in the wind tunnel and rotor blade level with a full-scale turbine experiment, and to prove a testing methodology for detecting the laminar to turbulent transition position on WT blades in operation.

The highest speed in the test section is about 120 m/s. The freestream TI in the test section ranges from 0.02% at an air speed of 10 m/s to 0.07% at 80 m/s, the speed at which the tests discussed herein were conducted. The glass-fiber airfoil model had chord of 0.6 m, span length of 1.25 m and TE thickness of 1 mm, and was mounted vertically in the 1.25 m-high, 1.8 m-wide octagonal test section with a streamwise length of 2.6 m. LE roughness was simulated by applying sandpaper to the airfoil LE. Sandpaper has a normalized size of its grain material designated by its grit number. This allows for repeatability of the experimental tests. The sandpaper sheet was installed with double-sided tape on the model. The sandpaper base sheet and coating have a finite thickness which may result in further aerodynamic effects that have to be taken into account. This is discussed in Section 5.2.

The model was instrumented with 63 pressure taps, staggered in the spanwise direction to avoid pressure readings being influenced by the upstream pressure taps. Lift and pitching moment were calculated by integrating the surface pressure distribution. Drag was calculated with a wake integral using the wake measurements of a static and total pressure rake placed at about 0.5 chords downstream of the model TE. The static wake rake had 16 static pressure taps, and the total pressure wake rake has 67 pressure tubes with varying spacing ranging from 3 mm over 96 mm in the rake centre to 6, 12 and 24 mm towards the ends of the rake. BL transition was measured using model-fitted microphones and IRT, but these measurements were not postprocessed and are therefore not considered in this study. Further information on the test rig and the measurement techniques is available in Pires et al. (2018).

Three rough LE models were obtained by by applying sandpaper of different grits, namely P240, P80 and P40. For each grit size, three coverage levels of the suction and pressure surface were considered, namely 4, 8 and 15% of the airfoil chord. Two reference conditions with tripped BL were also measured, tripping the BL with zigzag tape of 0.25 and 0.6 mm on both pressure and suction sides at a distance of $0.08c$ from the LE. The Delft test case considered in the analyses below consists of the clean airfoil and the roughened LE variant obtained by applying P40 sandpaper over $0.15c$ from the LE on the suction and pressure sides. The equivalent sand-grain roughness of the P40 sandpaper is $K_s \approx$ 425 µm, corresponding to a value of about 708 µm for a unitary chord. The Reynolds number Re based on the model chord is 3.0M.

3 Computational aerodynamics codes used in the benchmark

Most participants used Reynolds-Averaged Navier-Stokes (RANS) CFD codes, but two low-fidelity codes were also used. The RANS CFD codes are ANSYS Fluent, used by LU; EllipSys2D, used by DTU; OpenFOAM, used by CENER, NORDEX, AIST, TNO and IWES. This section summarizes the formulation of the turbulence and transition models used by most RANS codes considered herein. Alternative choices, along with roughness models adopted by each RANS code, are presented in dedicated subsections providing an overview of each RANS code. The last two subsections also briefly define the low-fidelity modeling approaches used by TNO and VESTAS, both based on the RFOIL code van Rooij (1996).

3.1 Turbulence and transition modeling

All RANS codes of this study use the two-equation $k-\omega$ Shear Stress Transport (SST) turbulence model Menter (1994); Menter et al. (2003) to model the impact of turbulence on the mean flow field of interest, and most RANS codes use the so-called $\gamma - Re_\theta$ SST four-equation model Menter et al. (2006); Langtry et al. (2006); Langtry and Menter (2009) to also account for wall BL transition. The latter model couples the two transport equations of the SST model to two additional transport equations defining a local correlation-based transition model (LCTM). The LCTM approach adopts empirical correlations relating local BL parameters, such as momentum thickness θ, and mean flow quantities, such TI and pressure gradient, to determine the onset of transition.

The $\gamma - Re_\theta$ SST model uses a transport equation for the turbulent intermittency γ. This variable is coupled with the SST turbulence model to activate and deactivate the production of turbulent kinetic energy k downstream of the transition area in the transport equation for k. A second transition-relevant transport equation for the 'transition onset momentum thickness Reynolds number' $\tilde{Re}_{\theta t}$ is also used. The use of this equation aims to account for the nonlocal influence of the TI, which changes due to the decay of k in the freestream and also due to variations of the flow velocity outside the airfoil BL. The $\tilde{Re}_{\theta t}$ equation links the empirical correlations used by the model to the onset criteria in the intermittency equation, and enables the use of the model for general geometries. The transport equations for γ and $\tilde{Re}_{\theta t}$ are, respectively:

$$\frac{\partial(\rho\gamma)}{\partial t} + \nabla\cdot(\rho\underline{v}\gamma) = P_\gamma - E_\gamma + \nabla\cdot\left[\left(\mu+\frac{\mu_t}{\sigma_f}\right)\nabla\gamma\right] \tag{1}$$

$$\frac{\partial\left(\rho\tilde{Re}_{\theta t}\right)}{\partial t} + \nabla\cdot\left(\rho\underline{v}\tilde{Re}_{\theta t}\right) = P_{\theta t} + \nabla\cdot\left[\sigma_{\theta t}(\mu+\mu_t)\nabla\tilde{Re}_{\theta t}\right] \tag{2}$$

where ρ, $\underline{v}$, μ and μ_t denote, respectively, density, velocity vector, molecular and eddy viscosity, and σ_f and $\sigma_{\theta t}$ are model constants Langtry and Menter (2009). The production term P_γ in Eq. (1) increases γ in the transition onset area and sustains it in turbulent regions of the BL; the destruction term E_γ enables modeling of BL relaminarization, by reducing the level of γ depending on the mean flow and the local BL conditions. The expression of P_γ and E_γ are available in Langtry and Menter (2009).

The production term $P_{\theta t}$ in Eq. (2) is given by:

$$P_{\theta t} = c_{\theta t}\frac{\rho}{t}\left(Re_{\theta t} - \tilde{Re}_{\theta t}\right)(1.0 - F_{\theta t}) \tag{3}$$

where t and $c_{\theta t}$ are a suitably defined time-scale and a model constant, respectively. The variable $Re_{\theta t}$ is determined with an empirical correlation depending on the local TI and Thwaites' pressure gradient coefficient λ_θ, defined as:

$$\lambda_\theta = \frac{\rho\theta^2}{\mu}\frac{d|\underline{v}|}{ds}$$

with $d|\underline{v}|/ds$ being the flow acceleration in the streamwise direction s Langtry and Menter (2009). The blending function $F_{\theta t}$ in Eq. (3) tends to 0 outside the BL, activating the source term $P_{\theta t}$ and forcing the transported variable $\tilde{Re}_{\theta t}$ to approach the value $Re_{\theta t}$ obtained with the empirical correlation. In the BL, $F_{\theta t}$ tends to 1, thus switching off the production of γ and enabling diffusion of $\tilde{Re}_{\theta t}$ between the BL edge and the wall boundary.

At each iteration of the solution process, the local value of $\tilde{Re}_{\theta t}$ is used to determine the critical Reynolds number $Re_{\theta c}$, the threshold above which the turbulence intermittency starts to increase in the BL. This is accomplished by using another empirical correlation of the form $Re_{\theta c} = f(\tilde{Re}_{\theta t})$ Langtry et al. (2006). When the local value of $\tilde{Re}_{\theta t}$ exceeds the threshold $Re_{\theta c}$, the model triggers production of intermittency via the P_γ source term in Eq. (1).

The production of intermittency attempts to model the transition process by forcing the source terms of the k-equation of the $k-\omega$ SST model to remain low before transition, and allowing it to progressively increase to its fully turbulent form as transition starts or progresses. The transport equations of k and the specific dissipation rate ω of this turbulence model Menter et al. (2003) are, respectively:

$$\frac{\partial(\rho k)}{\partial t} + \nabla\cdot(\rho\underline{v}k) = \tilde{P}_k - \tilde{D}_k + \nabla\cdot[(\sigma_k\mu_t+\mu)\nabla k] \tag{4}$$

$$\frac{\partial(\rho\omega)}{\partial t} + \nabla\cdot(\rho\underline{v}\omega) = P_\omega - D_\omega + \nabla\cdot[(\sigma_\omega\mu_t+\mu)\nabla\omega] + 2(1-F_1)\frac{\rho\sigma_{\omega 2}}{\omega}\nabla k\cdot\nabla\omega \tag{5}$$

where σ_k, σ_ω and σ_{ω_2} are model constants, and F_1 is a blending function of the $k-\omega$ and $k-\epsilon$ turbulence models. The changes brought about by LCTM in the SST transport equations are limited to a) the production term $\tilde{P}_k$ and the destruction term $\tilde{D}_k$ in Eq. (4), which are made to depend also on γ, and b) the blending function F_1 in Eq. (5), due to required additional robustness of this function when used in the framework of the $\gamma - Re_\theta$ SST model Menter et al. (2006).

The boundary conditions (BCs) for k and ω at wall and far-field boundaries are reported in Menter et al. (2003). The BC for γ at walls uses zero normal flux, whereas at far-field boundaries, γ is set to 1. The BC for $\tilde{Re}_{\theta t}$ at walls also uses zero normal flux. At far-field boundaries the value of this variable is calculated from the empirical correlation based on the inlet TI (Langtry et al., 2006).

The turbulent viscosity is computed using the equation

$$\mu_T = \frac{\rho a_1 k}{\max(a_1\omega, S F_2)} \tag{6}$$

where $a_1 = 0.31$ Menter et al. (2003). In some analyses of this study, however, a_1 has been set to a different value, which led to significant improvement of the agreement between computed and measured airfoil force data. Other studies also reported alterations of this coefficient prompted by similar observations (Zanon et al., 2018; Adeel-Ur-Rehman et al., 2024; Gutiérrez et al., 2024).

3.2 ANSYS Fluent (LU)

Fluent is a cell-centered finite volume RANS code using second-order space discretization of the convective, viscous and source terms of the RANS, turbulence and transition model equations. Turbulence and smooth wall BL transition modeling of the CFD analyses herein is based on the $\gamma - Re_\theta$ SST four-equation model. The constant a_1 has been set to 0.29 for all the analyses of the NACA 63_3-418 airfoil. For transitional smooth-airfoil simulations, the Kato-Launder modification of the k production term P_k in Eq. (4) is used (Kato and Launder, 1993). In both smooth- and rough-airfoil cases, the term P_k is limited with the limiter proposed in Menter (1993), by updating the production term of k taking the minimum between its destruction term and the value computed with the definition of this term multiplied by 10.

Rough-wall functions are used at rough surfaces to determine the wall shear stress accounting for the increase of this variable due to roughness. The general form of the rough-wall function is

$$u_+ = \frac{1}{\kappa}\ln y^+ + B - \Delta B\left(K_s^+\right) \tag{7}$$

in which $u^+ = u/u_\tau$, $y^+ = yu_\tau/\nu$, u is the velocity component parallel to the wall at distance y from the wall itself, ν is the kinematic viscosity and u_τ is the so called friction velocity. The friction velocity is given by $u_\tau = \sqrt{\tau_w/\rho}$, where τ_w is the shear stress at the wall. The values of the constants κ and B are $\kappa = 0.4$ and $B = 5.5$.

At smooth walls $\Delta B = 0$, whereas at rough walls ΔB is a function of the equivalent sand-grain roughness K_s Schlichting (1936), with the nondimensionalized form being $K_s^+ = K_s u_\tau/\nu$. Three main roughness regimes are typically considered: hydraulically smooth regime, characterized by roughness element height smaller than the viscous sublayer height and negligible impact on friction drag; transitionally rough regime, characterized by non-negligible pressure and viscous forces on the roughness element and added overall drag depending on the freestream Reynolds number, and fully rough regime, in which the additional friction drag is independent of the freestream Reynolds number and is caused predominantly by the pressure force on the roughness elements. According to Nikuradse (1950), the transitionally rough regime is defined by $3.5 < K_s < 68$. Other researchers proposed different K_s^+ ranges for the transitionally rough regime, and FLUENT uses $2.25 < K_s^+ < 90$ with the formulas proposed by Cebeci and Bradshaw (1977). In the transitionally rough regime ($2.25 < K_s^+ < 90$), ΔB is defined as:

$$\Delta B = \frac{1}{\kappa}\left[\ln\left(\frac{K_s^+ - 2.25}{87.75} + C_s K_s^+\right)\right]\sin\left[0.4258(\ln K_s^+ - 0.811)\right] \tag{8}$$

whereas in the fully rough regime ($K_s^+ > 90$), ΔB is calculated with the expression

$$\Delta B = \frac{1}{\kappa}\ln\left(1 + C_s K_s^+\right) \tag{9}$$

where C_s is a roughness-pattern dependent constant set to 0.5 in the analyses below.

The smooth airfoil FLUENT simulations below do not use wall functions. The turbulence and transition transport equations are integrated down to the wall, with the distance δ_w of the first cell center off the wall from the wall itself selected to fulfill the Reynolds number-dependent $\delta_w^+ < 1$ constraint for fully resolved BL analyses. At rough walls, the airfoil simulations below use the rough-wall function (7) to calculate τ_w. To accomplish this, δ_w^+ is increased by $K_s^+/2$ when $\delta_w^+ < K_s^+$ (virtual wall displacement).

3.3 EllipSys2D (DTU)

The incompressible flow solver EllipSys2D (Sørensen, 1995; Michelsen, 1992) uses structured grids and a cell-centered finite volume formulation with a multiblock approach for parallelization. It employs an efficient multigrid algorithm to solve the

https://doi.org/10.5194/wes-2026-89
Preprint. Discussion started: 3 June 2026

pressure-correction problem and grid sequencing for further convergence acceleration. The coupled momentum and pressure-correction equations are solved by using an improved version of the Semi-Implicit Method for Pressure Linked Equations-Consistent (SIMPLEC) algorithm (Kolmogorov et al., 2015), and the convective terms are discretized with the third-order accurate QUICK scheme (Leonard, 1979). All simulations presented herein use the $k-\omega$ SST turbulence closure, which is coupled to the e^N transition model (van Ingen, 1956; Smith and Gamberoni, 1956; Drela and Giles, 1987) in EllipSys2D (Michelsen, Jess A., 2002). The transition model is only active in the simulations of the clean airfoils. Distributed roughness effects are captured by the rough-wall model by (Knopp et al., 2009). Though usually this model avoids triggering the activation of the SST limiter within the viscous sublayer—in contrast to the one by (Wilcox, 1988)—the modification by (Hellsten and Laine, 1997) helps when running with extremely high roughness lengths.

When the grid has a O-shape topology, as in the present study, the in- and outflow BCs are applied dynamically depending on the AoA. The inflow conditions for the turbulent flow analyses are set according to Spalart and Rumsey (2007), with k_∞ derived from the freestream TI and $\omega_\infty = 5\ \mathrm{s}^{-1}$. Source terms for the turbulent quantities ensure that the eddy viscosity ratio does not dissipate away from the inflow (Spalart and Rumsey, 2007). They are deactivated within the BL using the indicator functions (F_1, F_2) of the SST model (Menter et al., 2003). The N factor is determined from the specified freestream inflow TI, following Mack (1977); the TI can be set independent of the actual far-field value use for the k-equation.

3.4 OpenFOAM

3.4.1 CENER models and settings

OpenFOAM, an open-source unstructured CFD toolbox based on the cell-centered finite volume method, was used for the RANS simulations reported below. The SIMPLEC algorithm was applied with an implicit relaxation factor of 0.9 for the pressure field and an explicit relaxation factor of 0.6 for the momentum and turbulence equations. Second-order discretization schemes were used for the gradient and Laplacian needed to calculate the face fluxes of the Navier-Stokes equations. For the momentum, turbulence and transition equations, a second-order accurate linear upwind scheme was used to calculate the advective fluxes. The convergence criterion of SIMPLEC, based on normalized residuals, required a decay below 1×10^{-7} for the pressure, momentum and turbulence equations. For the linear solvers, a 3-post-sweep V-cycle Geometric-Algebraic Multi-Grid (GAMG) solver combined with the *DICGaussSeidel* smoother was used to solve the pressure equation. For the momentum, turbulence, and transition equations, the *smoothSolver* algorithm with the *symGaussSeidel* smoother was used. For these linear solvers, an absolute tolerance of 1×10^{-14} and a relative tolerance of 1×10^{-2} were set for all equations.

The $\gamma - Re_\theta$ SST four-equation model described in Section 3.1 was employed for the transitional flow analyses of the clean airfoils under investigation.

An equivalent sand-grain roughness approach was implemented to account for the detrimental impact of surface roughness on airfoil aerodynamics, based on Wilcox's rough-wall BC (Wilcox (1988)). The model defines a roughness-dependent BC for the specific dissipation rate ω of the $k-\omega$ turbulence model as follows:

$$\omega_w = \frac{u_\tau^2}{\nu} S_R \tag{10}$$

with

$$S_R = \begin{cases} \left(\frac{50}{K_s^+}\right)^2 & \text{if } K_s^+ < 25. \\ \frac{100}{K_s^+} & \text{if } 25 \leq K_s^+ \leq 20000. \end{cases} \tag{11}$$

In addition, the correction of Hellsten and Laine (1997) was applied to the SST limiter of the $k-\omega$ SST turbulence model in rough-wall cases. This was accomplished by modifying Eq. (6) as follows:

$$\mu_T = \frac{\rho\, a_1\, k}{\max\left(a_1 \omega, S\, F_{23}\right)} \tag{12}$$

where $F_{23} = F_2$ for the case of smooth surfaces and $F_{23} = F_2 * F_3$ in the case of rough walls. Function F_3 is defined as:

$$F_3 = 1 - tanh\left[\left(\frac{150\nu}{\omega d^2}\right)^4\right] \tag{13}$$

where d denotes the distance normal to the wall.

A turbulence decay control method was implemented to prevent large, non-physical reductions of the k and ω variables of the $k-\omega$ SST turbulence model throughout the domain, based on Spalart and Rumsey (2007). The minimum k value was set to the value prescribed on the far-field boundary, whereas the minimum value of ω was set to 5 s^{-1} rather than the far-field value, to ensure stability. These limiters enable maintaining the TI prescribed at inflow far-field boundary until the airfoil LE and away from the airfoil's wake.

3.4.2 NORDEX models and settings

The RANS analyses reported below were performed using OpenFOAM version 9.0. The flow was modeled as incompressible and steady, and a second order space discretization was used for all equations. The SIMPLEC algorithm was selected for the numerical integration. The convergence criterion required that residuals of all flow variables fell below 1×10^{-6}. As a result, an average of 3,000 iterations were required to reach convergence. For the linear solvers, a 3-post-sweep V-cycle Geometric-Algebraic Multi-Grid (GAMG) solver combined with the *DICGaussSeidel* smoother was used to solve the pressure equation. For the momentum, turbulence, and transition equations, the *smoothSolver* algorithm with the *symGaussSeidel* smoother was used. For these linear solvers, an absolute tolerance of 1×10^{-14} and a relative tolerance of 1×10^{-2} were set for all equations.

In both the clean and rough airfoil simulations, the equations of the turbulence and transition models were integrated all the way down to the airfoil surface. The $\gamma - Re_\theta$ SST four-equation model described in Section 3.1 was employed for the flow analyses of the clean airfoils.

For the rough airfoils, fully-turbulent simulations were performed with the $k-\omega-SST$ turbulence model, along with the alterations of the boundary condition of ω at the wall and the calculation of the turbulent viscosity μ_t defined in Section 3.4.1.

The decay of k and ω between the far-field and the airfoil was estimated by means of the method of Spalart and Rumsey (2007). Following this approach, the values of k_∞ and ω_∞ were adjusted to make the TI level match that ahead of the airfoil measured in the wind tunnel.

https://doi.org/10.5194/wes-2026-89
Preprint. Discussion started: 3 June 2026

3.4.3 AIST models and settings

OpenFOAM, version v2106 of the OpenCFD distribution was used for the simulations reported below. The SIMPLE algorithm was applied with an implicit relaxation factor of 0.3 for the pressure field and an explicit relaxation factor of 0.7 for the momentum and turbulence equations. The gradient, convection, and diffusion terms were discretized using second-order schemes for all transport equations. The convergence criterion of SIMPLE required the absolute residual of the pressure equation to drop below 1×10^{-7} and that of all transport equations (momentum, turbulence and transition) to drop below 1×10^{-6}. The relative tolerances, i.e. the ratio of the final to initial residuals, for the linear solvers of the pressure and transport equations were set to 0.01 and 0.1, respectively. With regard to the linear solvers, a GAMG solver combined with the *GaussSeidel* smoother was used for the pressure equation. For the momentum, turbulence and transition equations, the *smoothSolver* algorithm with the *symGaussSeidel* smoother was used. The $\gamma - Re_\theta$ SST four-equation model is used for transitional flow simulations. Wall functions are applied to calculate the turbulent kinematic viscosity ν_t and the specific dissipation rate ω in near-wall flows for all simulations presented.

Above smooth wall regions, ν_t is calculated using the relation:

$$\nu_t = \nu_w \left[\frac{y^+ \kappa}{\ln\left(E y^+\right)} - 1 \right] \tag{14}$$

in the log-law region. If the first cell centre off the wall lies in the viscous sublayer, ν_t is set to zero. The value of the constants in Eq. (14) are $\kappa = 0.41$ and $E = 9.8$. At rough wall patches, E is replaced by E', with $E' = E$ for $K_s^+ < 2.25$ and $E' = E/f_n$ for $K_s^+ > 2.25$. The factor f_n is a function of K_s^+, and is given by the equation below:

$$f_n = \begin{cases} 1 + C_s K_s^+ & \text{for } K_s^+ \geq 90 \\ \left(\frac{K_s^+ - 2.25}{87.75} + C_s K_s^+ \right)^{sin\left(0.4258\left(ln\left(K_s^+\right) - 0.811\right)\right)} & \text{for } K_s^+ < 90 \end{cases} \tag{15}$$

where C_s is a roughness parameter set to 0.5 in this study.

The value of ω in the BL is estimated using the wall function blending the viscous sublayer contribution ω_{vis} and inertial layer contributions ω_{log}, based on a binomial function Menter and Esch (2001). According to this model, the value of ω in the BL is calculated using the relation:

$$\omega = \left(\left(\omega_{vis}\right)^2 + \left(\omega_{log}\right)^2 \right)^{0.5} \tag{16}$$

where $\omega_{vis} = \frac{6\nu_w}{\beta_1 y^2}$ and $\omega_{log} = \frac{k^{0.5}}{C_\mu \kappa y}$. The value of the constants in this equation are $\beta_1 = 0.075$ and $C_\mu = 0.09$.

3.4.4 TNO models and settings

The simulations were carried out using the steady-state incompressible `simpleFoam` solver, which employs the Semi-Implicit Method for Pressure-Linked Equations (SIMPLE) algorithm to couple velocity and pressure fields. The spatial discretization of the governing equations used the following methods: the momentum equations were discretized with the second-order bounded `Gauss linearUpwind` scheme; the equations of the $\gamma - Re_\theta$ SST model were discretized with the bounded

`Gauss limitedLinear` scheme, which switches to a first-order upwind scheme in regions of rapidly changing gradients to ensure numerical stability, while maintaining second-order accuracy elsewhere; the pressure equation was solved using the GAMG solver, which utilizes a `GaussSeidel` smoother for efficient convergence. Each simulation was taken to be converged when the root-mean-square (RMS) absolute residual for all equations was less than 10^{-7} or this RMS decreased by five orders of magnitude.

The rough LE analyses herein use a rough wall generalization of the $\gamma - Re_\theta$ SST model (Vimalakanthan et al., 2023), integrated in the OpenFOAM framework. This model is an alternative to rough-wall functions for incorporating surface roughness effects on BL transition, a modeling feature essential for predicting accurately the aerodynamic performance of airfoils in the presence of moderate LEE. The model introduces a new transport equation accounting for roughness amplification effects, encapsulated by a field variable A_r named 'roughness amplification'. This variable captures the downstream influence of surface roughness, effectively modifying the local correlation variable $Re_{\theta,t}$ in the $\gamma - Re_\theta$ SST transition model, enabling earlier transition to turbulence in the presence of LE roughness.

This five-equation transition model underwent extensive calibration using experimental data from Sandia's LEE study dataset (Maniaci and White, 2020) for the NACA 63_3-418 airfoil. Particular focus was placed on LE roughness heights between 100 to 200 µm. For roughness heights between 140 and 200 µm, the model showed excellent agreement with experimental data, accurately predicting aerodynamic forces. However, for smaller roughness heights (e.g. 100 µm), while the transition location was reasonably well-predicted, discrepancies between measured and computed aerodynamic forces were observed. This led to refinements in the calibration process, ensuring the model's robustness across a range of conditions.

3.4.5 IWES models and settings

The SIMPLEC algorithm was used for the integration of the governing equations, and second-order schemes were used for the space-discretization. For the linear solvers, GAMG combined with the Preconditioned Conjugate Gradient smoother was used to solve the pressure equation. For the momentum, turbulence, and transition equations, the *smoothSolver* algorithm with the *symGaussSeidel* smoother was used.

The $\gamma - Re_\theta$ SST four-equation model described in Section 3.1 was employed for the transitional flow analyses of the clean airfoils. The rough airfoil simulations assumed fully turbulent BLs, and the effect of roughness on the wall shear stress was modeled with a rough wall function of the type reported in Section 3.4.3. The constant a_1 in Eq. (6) was set to 0.29 for all the analyses of the NACA 63_3-418 airfoil.

A turbulence decay control method was implemented to prevent large, non-physical reductions of the k and ω variables of the $k - \omega$ SST turbulence model throughout the domain, based on Spalart and Rumsey (2007). The minimum k value was set to the value prescribed on the far-field boundary, whereas the minimum value of ω was set to $5\ s^{-1}$ rather than the far-field value, to ensure stability. These limiters enable maintaining the TI prescribed at inflow far-field boundary until the airfoil LE and away from the airfoil's wake.

3.5 RFOIL (TNO)

Sandia's low-order roughness model (Langel et al., 2017) was implemented in the 2D vortex panel code RFOIL (van Rooij, 1996). RFOIL is used extensively by the WT industry for airfoil design. The code was originally developed in 1996 by ECN, TU Delft and NLR as a "wind turbine modification" of the aerospace code XFOIL (Drela, 1989). The roughness model developed by Sandia aims at predicting the transition behavior of airfoils under a variety of roughness configurations. This model relies on an empirical correlation that was calibrated through the experimental data from the Texas A&M experiment (Ehrman, 2014). This correlation relates the integrated effect of surface roughness around the airfoil LE, which is defined by a nondimensional integrated roughness parameter, to a change in the transition onset momentum thickness Reynolds number. Rough LE analyses are performed by means of two RFOIL simulations. The transition position in rough-wall conditions is obtained from a smooth-wall RFOIL simulation, and the above-mentioned empirical correlation. The position of the transition point thus obtained is enforced in a subsequent RFOIL simulation to determine the aerodynamic polars accounting for rough-wall effects. The described methodology was used for the RFOIL analyses reported below.

3.6 DART (VESTAS)

DART (Digital Airfoil Reconstruction Tool) is a software that corrects simulated polar data, like those obtained with RFOIL simulations, to account for the aerodynamic impact of distributed and localized roughness due to erosion and other sources of geometry perturbations. The tool is based on extensive sets of wind tunnel data collected by Vestas over the years. These data sets enable to correlate directly the curves of lift, drag and moment coefficient to general geometry perturbations by means of measured data-based regressions.

4 CFD simulation set-ups

The results of all simulations reported below were obtained with steady flow analyses, and it was verified that the grids used for all CFD analyses reported herein provided mesh-independent results. The CFD analyses of most participants used the same grid for the clean and rough variant of the considered airfoil. The IWES (OpenFOAM) analyses, however, used slightly different grids for the clean and rough airfoil analyses. When the clean airfoil analyses resolved BLs all the way down to the airfoil surface, the selected height of the wall-adjacent cells δ_w resulted in the maximum value of the nondimensionalized wall distance δ_w^+ never exceeding 1 for all AoA values. For the analyses using smooth- or rough-wall functions, it was verified that δ_w^+ always lied in the logarithmic range of the turbulent BL. In all cases, it was ensured that the level of turbulence of the flow approaching the airfoil (about half a chord upstream of the LE) had the same order of magnitude measured in the wind tunnel experiments. For the CFD codes featuring an algorithm to minimize the turbulence decay between the inflow region of the far-field boundary, the prescribed turbulence level at the far-field boundary was equal or very close to that measured in the tests; for the other codes, a higher level of far-field turbulence was prescribed in order to achieve the desired turbulence level shortly ahead of the airfoil. Although all CFD codes, except for EllipSys2D, are unstructured, a structured grid topology was

https://doi.org/10.5194/wes-2026-89
Preprint. Discussion started: 3 June 2026

used by all simulations, with all grids consisting of quadrilateral cells. Grids of the O, C- and H-type were used. Key physical and numerical parameters of all CFD simulations are provided in Appendix A.

5 Results

This section considers the comparative analysis of the performance of the clean- and rough-LE variants of the NACA 63_3-418 airfoil based on the wind tunnel experiments and the simulations of all codes presented above. The section is made up of three parts. The first subsection focuses on the analyses of the NACA 63_3-418 airfoil of the Texas A&M experiment for moderate LE degradation, while the second subsection focuses on the analysis of the same airfoil tested in the Delft wind tunnel for severe LE degradation. The two experiments differ primarily by the level of LE roughness of the rough variant, which is significantly higher in the Delft experiment. The third subsection presents the comparative analyses of power and AEP losses of the NREL 5 MW WT based on the aerodynamic performance degradation of the NACA 63_3-418 observed at different level of LE roughness. The power and AEP loss analyses use the outcome of the experimental and numerical assessments of both the Texas A&M and the Delft experiments.

It is noted that all participants' CFD simulations of the NACA 63_3-418 airfoil of the Texas A&M experiment used the airfoil geometry of the actual model tested in the wind tunnel, which is available in the form a Bezier curve-based parametrized model. Conversely, the actual geometry of the model tested in the Delft experiment is not available and there have been some variations in the geometry used by the participants for the simulation of the Delft experiment.

5.1 Analyses of NACA 63_3-418 airfoil of Texas A&M experiment

Figure 2 presents the comparison of measured and computed force coefficients of the clean NACA 63_3-418 airfoil tested in the Texas A&M wind tunnel. Very good agreement of measured and all computed values of c_l is observed at AoA values between -3^o and 5^o (left subplot). Above 5^o, the CENER (OpenFOAM) c_l curve follows quite closely the measured curve and predicts well the measured peak c_l and the corresponding AoA. The Vestas (DART) prediction of the c_l curve also matches fairly well the measured curve over the entire AoA range considered, although it slightly underpredicts the c_l values in the stall and post-stall regimes. The remaining computed curves overpredict the measured c_l above α=5^o. Although some predictions follow more closely the measured curve up to about 10^o, they overpredict the measured AoA at which the measured maximum c_l, i.e. stall, occurs: the measured stall angle is about 11^o, whereas these simulations predict stall at 14^o or higher AoA values. The largest overprediction of c_l in the stall and post-all regions is that of AIST (OpenFOAM). Possible reasons for this discrepancy with respect to the CENER (OpnFOAM) result, which uses the same FD code, are the use of a higher value of the constant a_1 amd wall functions in the AIST approach. Higher values of a_1 lead to higher stall AoA and peak c_l, and the use of wall functions for the clean airfoil analysis may also reduce the prediction reliability in the stall area, where flow separation starts occurring.

Good agreement of measured and all computed values of c_d is obtained for AoA between -3^o and about 5^o (middle plot of Fig. 2). As the AoA increases, most simulations underpredict the measured drag, consistently with the delayed stall predictions highlighted in the analysis of the c_l curves. Also in this case, the CENER (OpenFOAM) prediction matches most closely the measured c_d curve over the entire AoA range considered. The Vestas (DART) prediction is in fair agreement with the measurements. From the stall AoA, the AIST (OpenFOAM) and DTU (EllipSys2D) analyses yield the largest underprediction of the measured c_d. The right plot of Fig. 2) compares the c_l/c_d curve obtained from the measured and computed values of c_l and c_d. Consistently with the observed variations in the curves of c_l and c_d, the largest scatter of the predicted c_l/c_d curves is observed for $\alpha > 5^o$. The scatter in the predictions of the highest efficiency is significant, with predicted maxima varying between about 90 and 130 against a measurement-based estimate of about 100.

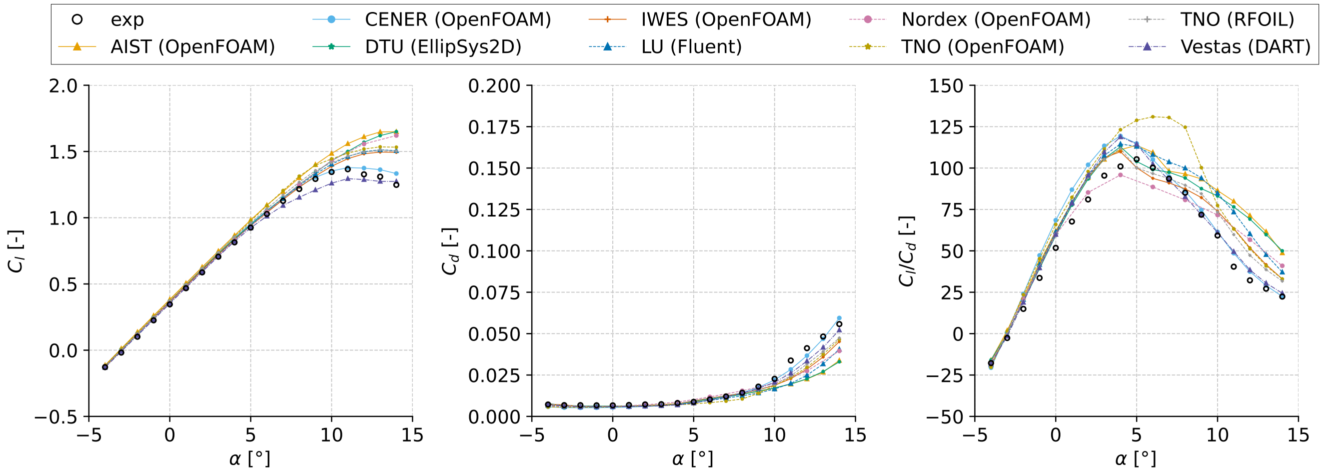

(a) (b) (c)

Figure 2. Comparison of measured data and computed results of the clean NACA 63_3-418 airfoil of the Texas A&M experiment: (a) lift coefficient c_l against AoA α; (b) drag coefficient c_d against AoA α; (c) ratio c_l/c_d against AoA α.

The dependence of the chordwise position of the BL transition on the AoA α for the clean airfoil suction side (SS) and pressure side (PS) is analyzed in Fig. 3's left and right plots, respectively. No measured values of the BL transition on the PS was available for this experiment. The predicted chordwise position of transition is obtained by taking the point with maximum slope of the curve of the skin friction coefficient c_f extracted by the simulations. This is because the c_f profile experiences a relatively sharp rise in the transition region. The measured position of transition was instead determined by means of infrared thermography. The left plot of Fig. 3 shows fairly good agreement between most predictions and measured data. For most predictions, the largest difference between predicted and measured position of the transition is lower than about 5% of the chord, with the DTU (EllipSys2D) prediction being closest to measurements. With regard to the analysis of transition, the main difference between the EllipSys2D set-up and that of all other codes is that the former code uses the e^N method to predict transition, whereas all other CFD code use the $\gamma - Re_\theta$ transition model, as indicated in Tab. A1. Hence, this result may indicate that the e^N method performs better than the $\gamma - Re_\theta$ method for this particular test case. The prediction furthest away

https://doi.org/10.5194/wes-2026-89
Preprint. Discussion started: 3 June 2026

from both measured data and all other simulations is that of TNO (OpenFOAM). The reason for this discrepancy is unclear and remains a matter of future investigation. On the PS (right subplot of Fig. 3), the scatter of the numerical predictions is unexpectedly larger than on the SS. Nevertheless, the overall trends are similar for most codes: the position of the BL transition moves towards the TE as the AoA increases, and the rate at which this happens decreases at an AoA of about 0°.

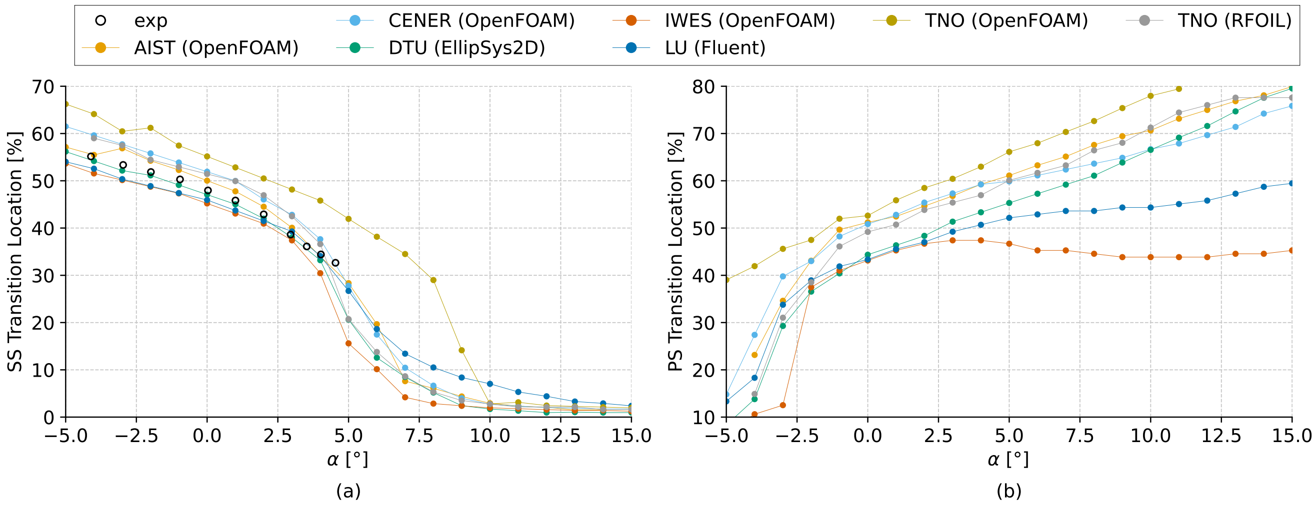

(a)

(b)

Figure 3. Comparison of measured data and computed results of the clean NACA 63_3-418 airfoil of the Texas A&M experiment: (a) SS chordwise position of transition against AoA α; (b) PS chordwise position of transition against AoA α.

Figure 4 compares measured and computed force coefficients of the NACA 63_3-418 airfoil with rough LE tested in the Texas A&M wind tunnel. The LE roughness is characterized by an equivalent sand-grain roughness K_s of 101 µm per meter chord. The choice of the ratio K_s/K yielding K_s=101 µm is discussed in Langel et al. (2017).

Inspection of the left subplot of Fig. 4 reveals overall good agreement of measured and all computed values of c_l, particularly for the CENER (OpenFOAM), AIST (OpenFOAM), LU (Fluent) and IWES (OpenFOAM) simulations. These four simulations predict fairly well also the stall and post-stall c_l curve regions. For α >8°, the other simulations tend to overpredict the measured c_l values. Interestingly, the measured c_l curve of Fig. 4 is quite similar to the measured curve of the clean airfoil in Fig. 2. In the post stall region, the measured c_l values of the airfoil with low-level roughness are slightly higher than those of the clean airfoil, pointing to a possible performance benefit due to small roughness in this region. This aspect is analyzed in further detail below.

Good agreement of measured and all computed values of c_d is observed between -3° and about 5° (middle plot). As the AoA increases, most simulations tend to underpredict the total drag, similarly to the clean airfoil case, with the numerical predictions now closest to the measurements being those of CENER (OpenFOAM), LU (Fluent), IWES (OpenFOAM) and Vestas (DART). The differences between measured and computed c_d curves are smaller than in the clean airfoil case. It is also noted that, as expected, the overall level of measured and computed c_d curves is higher than that of the clean airfoil. The right subplot of Fig. 4 reports the comparison of the ratio c_l/c_d using measured and computed values of c_l and c_d. Similarly to the clean airfoil case, the scatter of the predictions after the AoA of peak efficiency is larger than before this reference angle. However the scatter of the computed curves is notably lower than for the clean airfoil case, consistently with the overall better predictions of the c_l and c_d curves of all codes. The closest agreement with the measurement-based curve is achieved by the CENER (OpenFOAM) simulation.

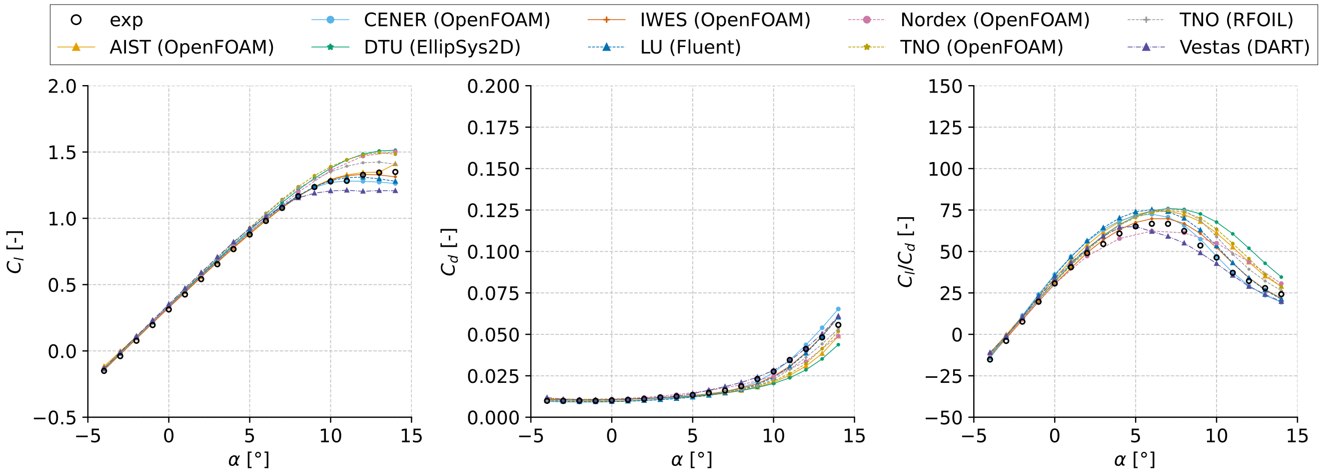

(a) (b) (c)

Figure 4. Comparison of measured data and computed results of the rough NACA 63_3-418 airfoil of the Texas A&M experiment: (a) lift coefficient c_l against AoA α; (b) drag coefficient c_d against AoA α; (c) ratio c_l/c_d against AoA α.

The differences between the rough and clean airfoil c_l, c_d and c_l/c_d based on the wind tunnel measurements and the simulations are reported in the three subplots of Fig. 5. The c_l drop Δc_l predicted by most simulations is comparable to the measured one for $\alpha < 8°$, and is smaller than 0.1. Only the AIST (OpenFOAM) set-up predicts a significantly higher c_l drop, due to its notable overestimate of the measured c_l of the clean airfoil. Below $\alpha = 11^o$, all CFD codes, except EllipSys2D, predict a c_l reduction larger than the measurements, with the measured c_l drop at $\alpha = 11°$ amounting to slightly less than 0.1. Above $\alpha = 11°$, the slope of the measured Δc_l curve becomes positive and from $\alpha = 12°$, the measured Δc_l values are positive, pointing to apparent benefits of low-level roughness on c_l in the post-stall regime. For $\alpha < 10°$, the closest agreement of measured and computed Δc_l is obtained by the Nordex (OpenFOAM) set-up. As for the c_d increase Δc_d, reported in the middle plot of Fig. 5, most computed values of Δc_d are relatively close to the measurement-based value of about 0.05 for $\alpha < 10°$. Also in the case of the Δc_d parameter, the closest agreement of measurements and simulations is obtained by the Nordex (OpenFOAM) set-up. Above $\alpha = 11°$, the computed data scatter increases. Consistently with the measured positive Δc_l in this AoA range, the measured drag loss decreases, getting close to zero, whereas all computed estimates tend to increase with AoA. The curves of $\Delta c_l/c_d$ in the right subplot are consistent with these observations. In general, all computed reductions of c_l/c_d are larger than the measurement-based values, due to all simulations overestimating to a minor or greater extent the drag increase due to moderate LE roughness. Interestingly, despite AIST (OpenFOAM) showing the largest overprediction of the c_l reduction due to LE roughness, the largest overprediction of the reduction of the c_l/c_d ratio is produced by TNO (OpenFOAM). This is because of the larger weight of Δc_d on the estimate of $\Delta c_l/c_d$. This aspect is important to WT power and AEP loss estimates and is analyzed in further detail in section 5.3.

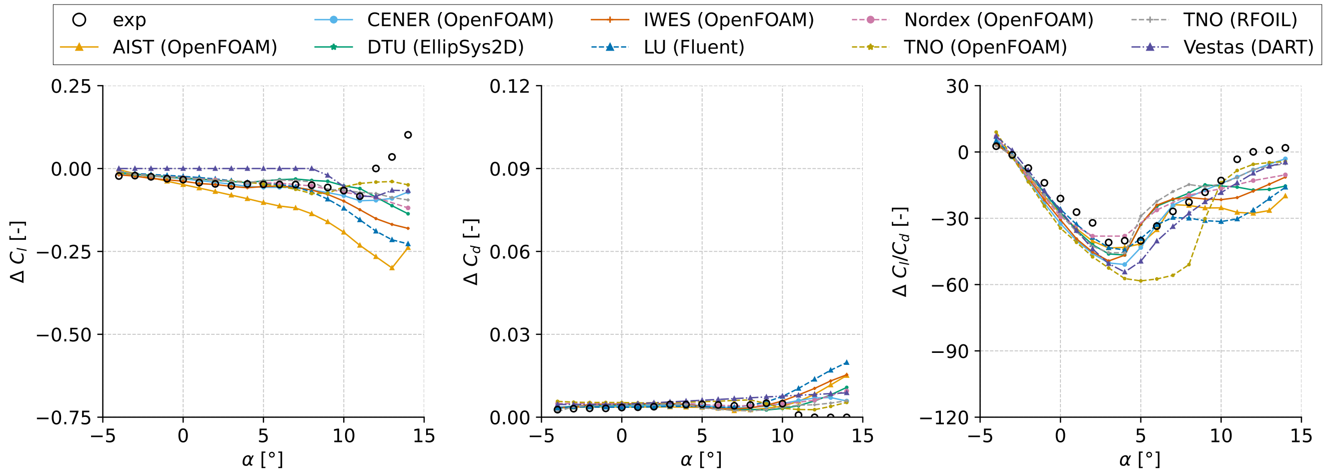

(a) (b) (c)

Figure 5. Comparison of measured and computed aerodynamic performance difference of clean and rough NACA 63_3-418 airfoils of the Texas A&M experiment: (a) lift coefficient difference Δc_l against AoA α; (b) drag coefficient difference Δc_d against AoA α; (c) difference $\Delta(c_l/c_d)$ against AoA α.

Figures 6 and 7 present the comparison of measured and computed profiles of airfoil static pressure coefficient c_p at $\alpha = 0°$ (left plots) and $\alpha = 10°$ (right plots) for the clean and rough airfoils, respectively. Overall good agreement of measurements and simulations is observed at both AoAs for the clean airfoil case. The difference among computed c_p profiles are quite small, even at $\alpha = 10°$, despite some differences among the predicted c_l values at this AoA. Figure 6 shows that all computed curves at $\alpha = 0°$ have a constant downward shift with respect to the measured profile. This offset may also exist in the comparison of the profiles at $\alpha = 10°$, but may appear less pronounced due to a wider range on the vertical axis. This offset could be due to an issue in the definition of the reference pressure for postprocessing the measured data. The discrepancy may also be due to some misestimate of the effective AoA obtained from wind tunnel corrections.

In the case of the rough airfoil (Fig. 7), the agreement of measured and computed c_p profiles is also very good. At $\alpha = 10°$, however, the differences among computed c_p profiles are larger than in the case of the clean airfoil, consistently with a larger scatter in the predicted c_l at this AoA, as seen in Fig. 4. At $\alpha = 0°$, the same downward shift of the computed profiles with respect to the measured profile discussed in the clean airfoil case is observed also in the rough airfoil analysis.

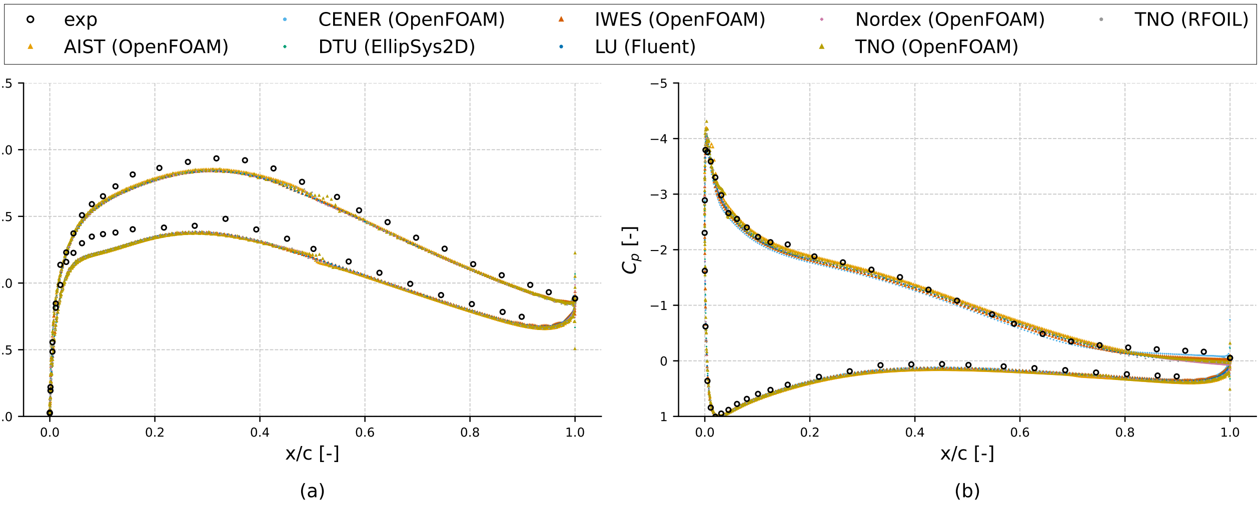

Figure 6. Comparison of measured and computed profiles of the clean NACA 63_3-418 airfoil static pressure coefficient c_p of the Texas A&M experiment: (a) AoA α=0°; and (b) AoA α=10°.

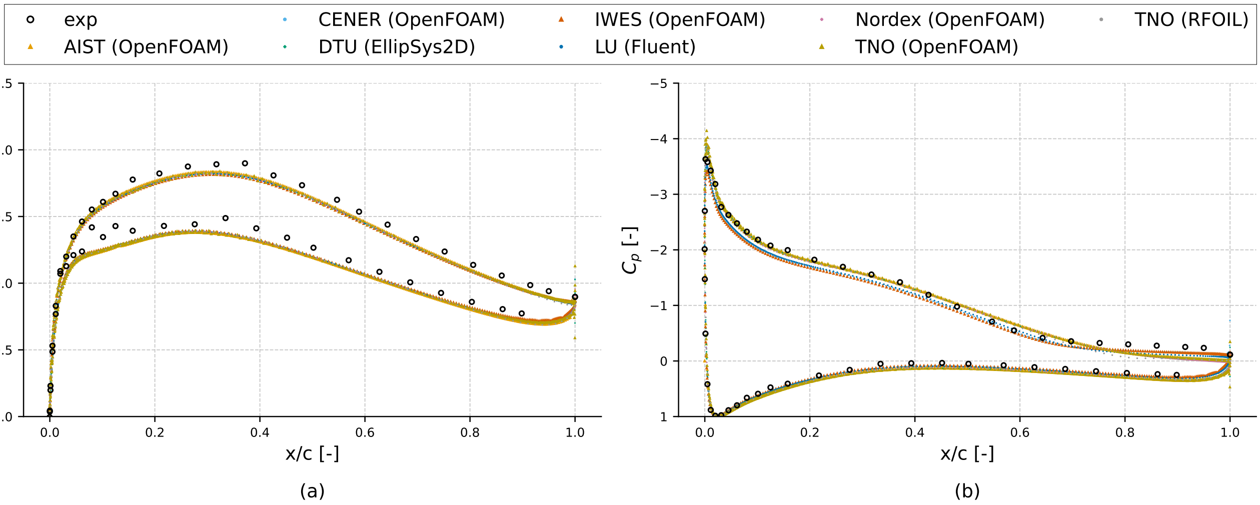

Figure 7. Comparison of measured and computed profiles of the rough NACA 63_3-418 airfoil static pressure coefficient c_p of the Texas A&M experiment: (a) AoA α=0°; and (b) AoA α=10°.

5.2 Analyses of NACA 63_3-418 airfoil of Delft experiment

Figure 8 presents the comparison of measured and computed force coefficients of the clean NACA 63_3-418 airfoil tested in the Delft wind tunnel. Comparing the measured c_l curves of Figures 8-a and 2-a highlights some differences between the Delft and Texas A&M experimental data: in the former case, the c_l curve is shifted slightly downwards, the peak c_l occurs at 10^o rather than at 12^o and the c_l curve after stall is flatter. These differences may be due to slightly different shape of the airfoil model in the two experiments due to manufacturing and/or mounting in the facility and/or small difference of TI levels in the wind tunnel.

The trends of agreement between measured data and computed results visible in Fig. 8 are similar to those discussed for the Texas A&M experiment. Overall good agreement of measured and computed values of the c_l curves is observed at values of AoA between -3^o and 5^o (left subplot), although the difference between measurements and several simulations has slightly increased with respect to the Texas A&M experiment. This is partly due to the downward shift of the c_l curve. The larger differences among the computed c_l curves are due to the fact that the geometry of the tested airfoil model is not available, and participants used slightly different airfoil geometries for the numerical analyses. Up to about 11^o, the LU (Fluent) c_l curve is the prediction closest to the measurements, and above this AoA the CENER (OpenFOAM) c_l curve is instead closest to measurements. For $5° < \alpha < 10°$, the TNO (OpenFOAM) estimate differs most from the measurements, whereas for $\alpha > 11°$ the largest difference is that of AIST (OpenFOAM). The remaining computed curves overpredict to a slightly minor extent the measured c_l above 5^o, but the overprediction is slightly larger than for the Texas A&M clean airfoil.

Good agreement of measured and computed values of the c_d is obtained for AoA between -3^o and about 5^o (middle plot of Fig. 8). The underprediction of measured c_d by several simulations is slightly larger than in the Texas A&M case. As the AoA increases, the c_d underprediction of all codes increases further, and is larger than than seen in the case of the clean airfoil of the Texas A&M study. Also in this case, the Vestas (DART) and the CENER (OpenFOAM) predictions match most closely the measured c_d curve over the entire AoA range considered, whereas the AIST (OpenFOAM) is farthest.

The right plot of Fig. 8) shows the ratio c_l/c_d based on measurements and simulations. The largest difference between measured and computed c_l/c_d estimates is that of the AIST (OpenFOAM) simulation. This is due to this set-up yielding the largest overprediction of c_l and the largest underprediction of c_d. For $5° < \alpha < 10°$ The TNO (OpenFOAM) prediction is also rather far from the measurements-based data, partly due to overprediction of c_l in the same AoA range. The trends and relative differences of all other simulations are very similar to those observed in the Texas A&M clean airfoil case.

Figure 9 compares measured and computed force coefficients of the NACA 63_3-418 airfoil with rough LE tested in the Delft wind tunnel. The LE roughness corresponding to the properties of the P40 sandpaper is characterized by an equivalent sand-grain roughness K_s of 425 µm. Since the chord of the airfoil model is 0.6 m, this results in a ratio K_s/c of about 708 µm/m.

Inspection of the left plot of Fig. 9 reveals a notably larger data scatter than observed for the rough airfoil of the Texas A&M analysis considered in Fig. 4. These differences are partly due to the aforementioned small differences in the airfoil geometry used by the participants. The simulations that best match the measured c_l curve over the whole AoA range considered

https://doi.org/10.5194/wes-2026-89
Preprint. Discussion started: 3 June 2026

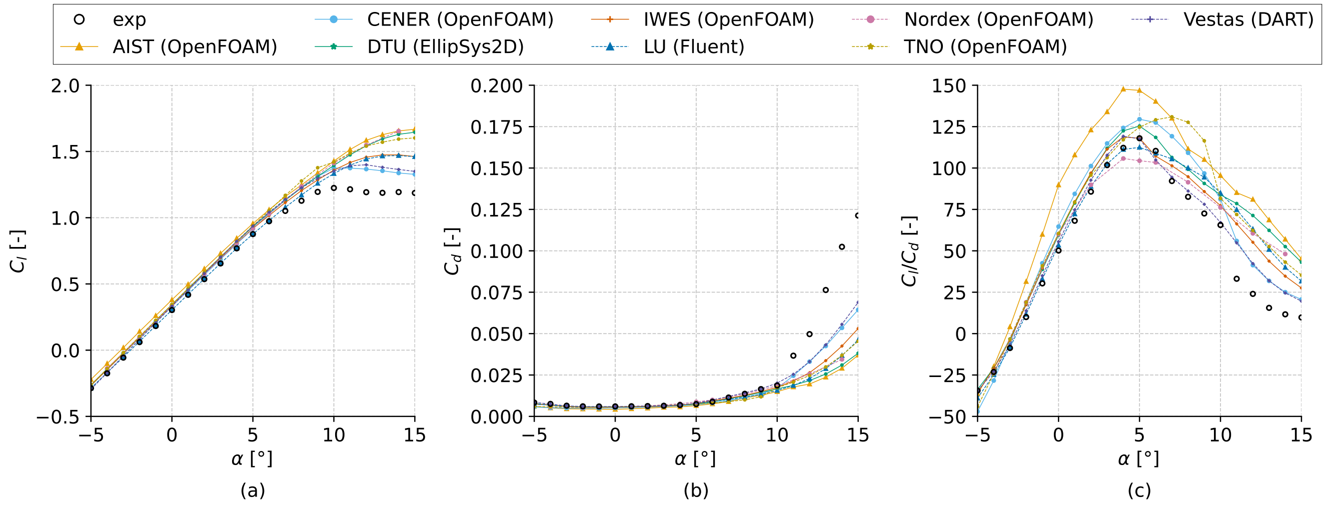

(a) (b) (c)

Figure 8. Comparison of measured data and computed results of the clean NACA 63_3-418 airfoil of the Delft experiment: (a) lift coefficient c_l against AoA α; (b) drag coefficient c_d against AoA α; (c) ratio c_l/c_d against AoA α.

are LU (Fluent), DTU (EllipSys2D) and IWES (OpenFOAM), whereas those farthest away are the Vestas (DART), AIST (OpenFOAM) and TNO (OpenFOAM). An additional possible reason for this large variability on the computed results is that, except for the Vestas (DART) set-up, which uses data regression for its estimates, several of the simulation codes use different values of the surface roughness corresponding to the P40 sandpaper. Most CFD simulations use a value of K_s significantly higher than that of the P40 sandpaper, and this was done to account for the impact of the backward facing step at either end of the applied sandpaper resulting from the thickness of the base and double-sided adhesive tape used for the application. Since this additional thickness is unknown, additional uncertainty resulted from different assumptions made by several simulation set-ups, as noticed in Tab. A3. In general, all simulations overestimate, to a greater or lesser extent, the c_l curve of the airfoil with high LE roughness. Nevertheless, most simulations predict stall inception in the AoA range between 10º and 13º, not too dissimilarly to the measured value of 10º. Comparing the measured c_l curves of the clean airfoil (Fig. 8) and the rough airfoil (Fig. 9), it is evident that the high level of roughness of the Delft experiment reduces significantly the peak c_l, from about 1.2 in the clean configuration to about 1.0 in the rough configuration.

At the considered high level of LE roughness, the measured c_d curve has higher values than in the Texas A&M experiment, as noted by comparing the measured curves of the middle plot of Figures 9 and 4. In the former case c_d at $\alpha = 5°$ amounts to 0.02 and in the latter to just about 0.012. In the considered case of high LE roughness, the spread of the numerical predictions for $\alpha < 5°$ is larger than in the lower roughness case, with the DTU (Ellipsis2D) and Nordex (OpenFOAM) simulations yielding the largest c_d overestimate, and the CENER (OpenFOAM) simulation yielding the largest underestimate of the c_d curve. These differences are most likely due to different choices of overall roughness magnitude in the simulation set-ups, but also differences in the models adopted by different codes (e.g. Cebeci-Bradshaw or Knopp model for the rough wall shear stress, different dimensional cell heights of wall cells). For $\alpha > 9°$, all simulations underpredict the total drag, with the predictions now closest to the measurements being those of DTU (EllipSys2D) and AIST (OpenFOAM). In contrast with the low roughness case of the Texas A&M campaign, the differences between measured and computed c_d curves for the higher roughness case of the Delft campaign are larger than in the clean airfoil case, and the data scatter is also more significant. The overall larger difference between measurements and simulations may be due to the flow perturbation associated with the base of the sandpaper being more significant than considered by all simulations, none of which resolves the backward facing step generated by the supporting layers of the sandpaper. It is also noted that, as expected, the overall level of measured and computed c_d curves is notably higher than that of the clean airfoil.

The measurement- and simulation-based c_l/c_d curves for the higher roughness level are reported in the right subplot of Fig. 9. Except for the CENER (OpenFOAM) result, most other predictions are relatively close to the measured curve for $\alpha < 8°$. It is noted, however, that for calculating power and AEP losses of WT with blade LE degradation, obtaining the correct ratio c_l/c_d is not the most relevant requirement, since these losses depend on the specific values of c_l and c_d, rather than on their ratio.

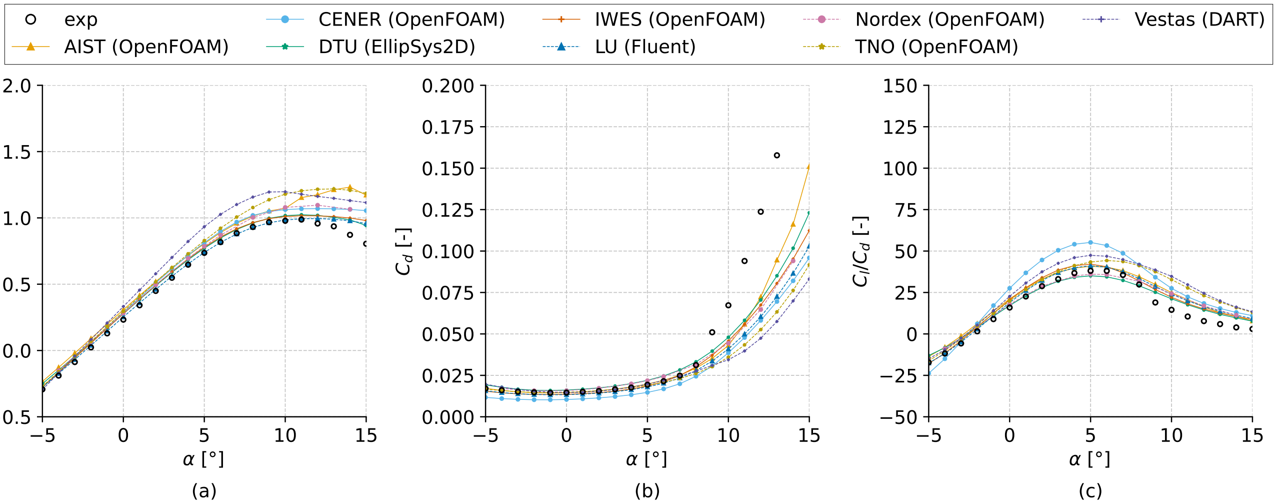

(a)

(b)

(c)

Figure 9. Comparison of measured data and computed results of the rough NACA 63_3-418 airfoil of the Delft experiment: (a) lift coefficient c_l against AoA α; (b) drag coefficient c_d against AoA α; (c) ratio c_l/c_d against AoA α.

The differences between the rough and clean airfoil c_l, c_d and c_l/c_d based on the wind tunnel measurements and the simulations of the Delft experiment are reported in the three subplots of Fig. 10. It is believed that the variability of these differences among codes is not strongly affected by the possible small differences in the actual geometry of the NACA 63_3-418 airfoil used in the simulations and the wind tunnel experiment, partly because the same airfoil geometry is used for clean and rough

LE analyses in all cases. Comparing these results with those of the lower roughness experiment in Fig. 5, one notes that both the c_l reduction and the c_d increase are notably higher in the Delft experiment. The Δc_l values predicted by most simulations are comparable to the measured ones for $\alpha < 8°$ and they reach a level of 0.2. Above $\alpha = 8°$, all codes predict c_l reduction much larger than those based on measurements. This is because in the stall and post-stall region, the c_l overestimate of the clean airfoil is notably larger than the c_l overestimate of the rough airfoil for most codes. As for the c_d increase, reported in the middle plot of Fig. 10, most computed values of Δc_d for $\alpha < 8°$ are relatively close to the measurement-based values, which reach about 0.15 at $\alpha \approx 8°$; exception to this is the CENER (OpenFOAM) prediction, which significantly underpredicts the c_d increase. Above this AoA, the data scatter increases notably. Quite interestingly, at high AoA, the predicted drag reduction of all simulations is lower than than that based on the measurements. The opposite was instead observed for the case of low LE roughness considered in the middle plot of Fig. 5.

The computed curves of $\Delta c_l/c_d$ (right subplot) are relatively close to the measurement-based estimate, except for the AIST (OpenFOAM), TNO (OpenFOAM) and DTU (EllipSys2D) estimates, which significantly overestimate the efficiency loss, due to overly pessimistic predictions of the c_l and c_d variations. Except for the case of the aforementioned three estimates, it is observed that the overestimate of the measurement-based c_l/c_d reduction predicted by most other simulations is larger for $\alpha > 5°$ than at lower AoA values. This is due to these simulations overestimating, to a greater or lesser extent, the lift reduction due to high LE roughness. The predicted lift reduction appears to dominate on the resulting ratio c_l/c_d, since at high AoA all simulation predict a smaller drag increase than the measurements.

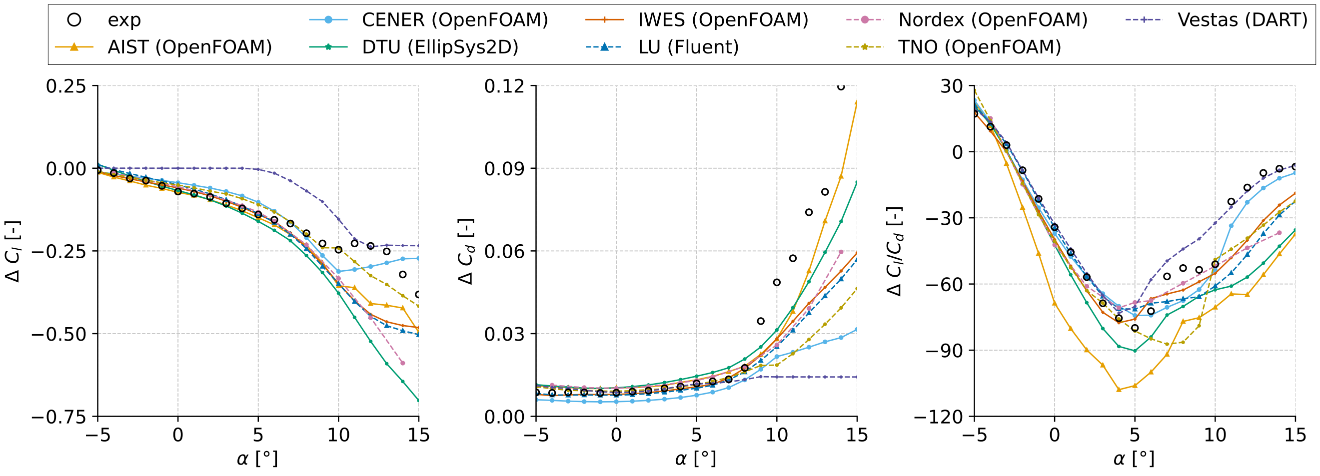

(a)

(b)

(c)

Figure 10. Comparison of measured and computed aerodynamic performance difference of clean and rough NACA 63_3-418 airfoils of the Delft experiment: (a) lift coefficient difference Δc_l against AoA α; (b) drag coefficient difference Δc_d against AoA α; (c) difference $\Delta(c_l/c_d)$ against AoA α.

Figures 11 and 12 compare measured and computed surface c_p profiles at $\alpha = 0°$ (left subplots) and $\alpha = 10°$ (right subplots) for the clean and rough airfoils, respectively. In the clean airfoil case, very good agreement between measured and computed data is observed at $\alpha = 0°$. At $\alpha = 10°$, the agreement is still reasonable, but the measured c_p profile on the suction side flattens up earlier than the computed profiles, and, before this plateau in the TE region, it is steeper than the calculated profiles. This is due to all simulations predicting stall-induced separation at an AoA larger than that observed in the measurements. In the case of the rough airfoil, the agreement of measurement and simulations at $\alpha = 0°$ is also very good. At $\alpha = 10°$, the agreement of measured and computed c_p profiles is even better than that observed for the clean airfoil at the same AoA, except for the TNO (OpenFOAM) analysis. The better general agreement is consistent with the fact that in the case of the rough airfoil the predicted c_l curves are closer to the measured data than they are in the case of the clean airfoil.

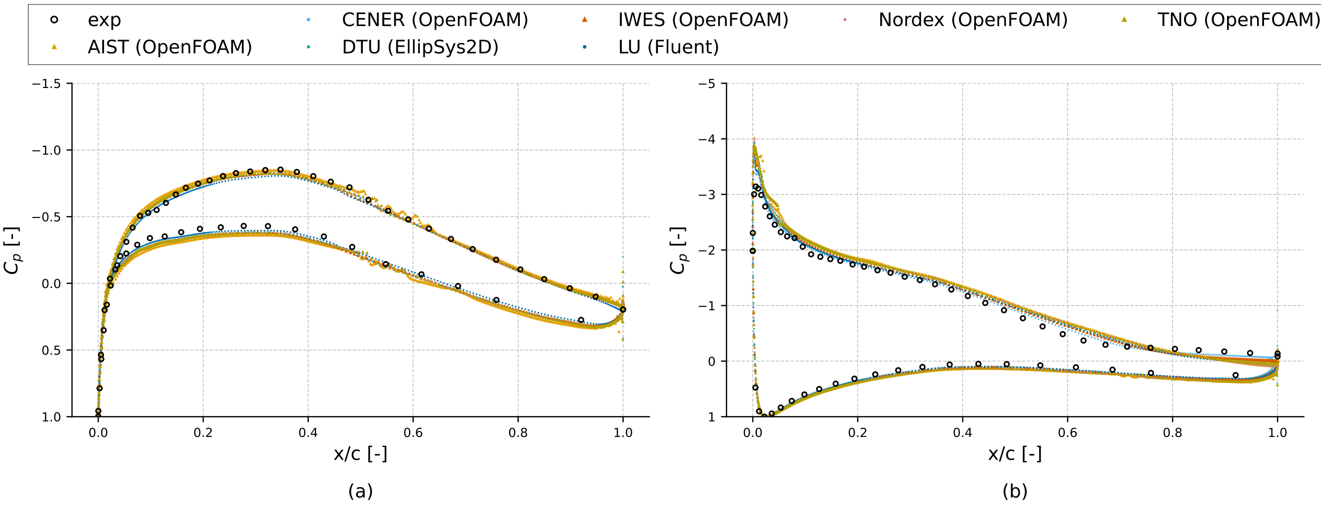

(a)

(b)

Figure 11. Comparison of measured and computed profiles of the clean NACA 63_3-418 airfoil static pressure coefficient c_p of Delft experiment: (a) AoA α=0°; and (b) AoA α=10°.

5.3 Power curve degradation and AEP loss at offshore and onshore sites

In order to assess the impact of the differences among code predictions of the NACA 63_3-418 airfoil featuring different levels of LE degradation on the reduction of power output and AEP, a modified version of the NREL 5 MW turbine Jonkman et al. (2009) is considered. The blade of the modified nominal turbine is obtained by replacing the NACA 64_3-618 airfoil, the original airfoil used by this turbine from about 70% rotor radius to the blade tip, with the NACA 63_3-418 airfoil. The rest of the blade geometry is that of the original NREL 5 MW turbine. The roughness cases are applied uniformly across the area of the blade where the NACA 63_3-418 airfoil has been applied (outer 30% blade span) to aid in comparison of the AEP loss predicted by the different models relative to the experimental results; the actual spanwise distribution of erosion damage measured in the

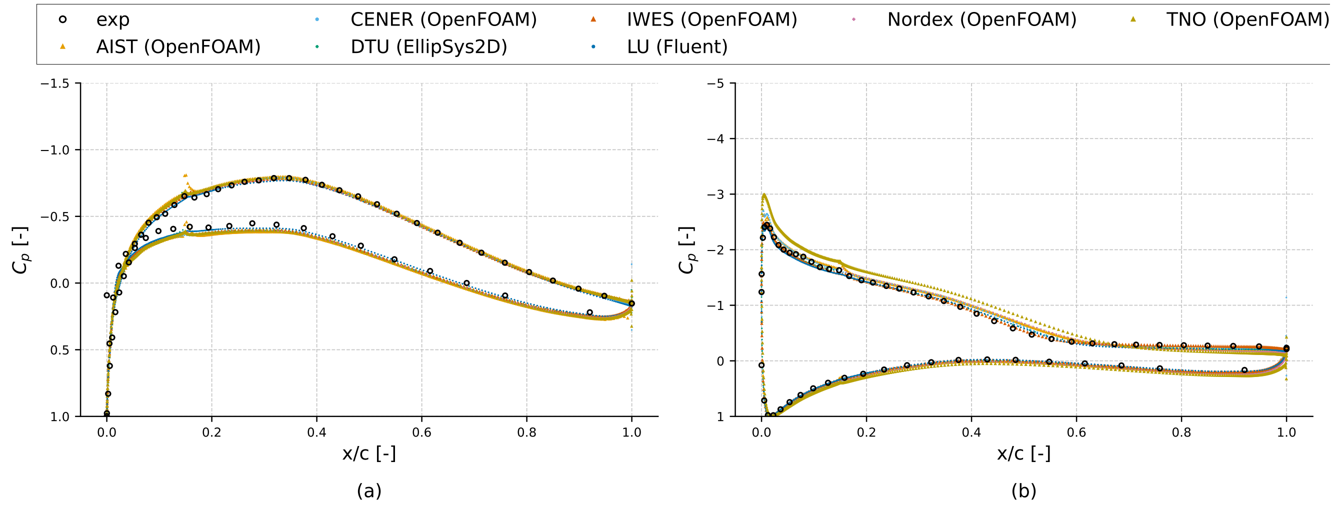

Figure 12. Comparison of measured and computed profiles of the rough NACA 63_3-418 airfoil static pressure coefficient c_p of the Delft experiment: (a) AoA α=0°; and (b) AoA α=10°.

field tends to be exponential and more realistic representations of this damage have been predicted to have approximately half the AEP loss as the method with constant spanwise distribution used in the comparison below (Maniaci et al., 2025).

An onshore site in Southern Italy and an offshore site in the North Sea are considered for the analysis of the power and AEP loss. The wind speed at the onshore site refers to a modified hub height of 100 m, whereas that at the offshore site refers to the original 90 m hub height of the 5 MW WT. The hub height of the onshore WT is greater than that of the offshore WT to increase the energy capture, partly compensating for lower wind speeds at hub height compared to offshore sites. The scale factor c and the shape factor k of the Weibull Probability Distribution Function (PDF) of the hub-height mean wind speed at the two sites, along with the annual mean wind speed V_{mean}, are reported in Tab. 1; further related information can be found in Castorrini et al. (2023). The table also reports the values of the shear exponent γ adopted to characterize the vertical gradient of the horizontal component of the wind speed at the two sites.

Table 1. Scale factor c and shape factor k of Weibull PDF of hub-height mean wind speed at offshore and onshore site, along with hub-height mean annual wind speed V_{mean} and shear exponent γ.

Site	c [m/s]	k [-]	V_{mean} [m/s]	γ [-]
Offshore	10.56	2.00	9.36	1/7
Onshore	8.83	1.88	7.84	1/5

The wind TI also impacts on WT AEP, as this parameter affects both the power curve between cut-in and rated wind speeds (Bardal and Sætran, 2017) and the power losses due to LE degradation between the same two characteristic wind

https://doi.org/10.5194/wes-2026-89
Preprint. Discussion started: 3 June 2026

speeds (Campobasso et al., 2023). The mean wind speed-dependent TI values for the offshore site are those measured by the FINO 1 met mast in the North Sea (Berge et al., 2009; Emeis, 2014), whereas the TI values used for the onshore site are those of the onshore wind of class B in the guidelines of the International Standard IEC61400. Further information on the adopted TI data is available in Castorrini et al. (2023).

For each mean wind speed considered in the WT analyses below, the required time-series of the inflow wind maps have been generated with the TurbSim code (Jonkman and Kilcher), using as input both the aforementioned site- and mean wind speed-dependent TI profiles and the wind shear exponents in Tab. 1.

The aero-servo-elastic WT analyses for determining power and AEP metrics have been performed with OpenFAST (Jonkman and Sprague) version 4.1.2, and structural deformations have been resolved using the ElastoDyn module. For both offshore and onshore simulations, the time step of OpenFAST was set to 0.01 s and the WT operation was considered for 630 s for each mean wind speed. The mean value of all variables was calculated after removing the first 30 s of the analyses.

Figure 13 analyzes the power variations due to moderate LE degradation of the NACA 63_3-418 airfoil assessed in the Texas A&M experiment. The figure reports the power curve of the modified reference WT based on the measured force coefficients of the clean airfoil, the curve of the percentage power loss based on the measured force coefficients of the clean and degraded airfoil, and the power loss curve based on the force coefficients of the same two airfoils computed with the simulation codes presented in Section 3. The left and right plots, in which V denotes the mean wind speed, refer to onshore and offshore TI, respectively. The power curve of the nominal WT obtained by using the measured force coefficients of the clean NACA 63_3-418 airfoil, is to be read on the left axis, whereas the curves of the percentage power loss, obtained with measured or computed force coefficients, are to be read on the right axis. The power loss curves, reporting the difference between the power of the nominal WT and that of the WT with moderate LE degradation, are based on either measured or computed airfoil data; for both data type, the power difference is normalized by the power of the nominal WT determined with the force coefficients of the clean airfoil acquired with the same method as the data for the difference (measurements or simulations).

The data of the left plot of Fig. 13 (onshore TI) show that the mean power loss predicted by using the measured and the computed force coefficients of most aerodynamic codes for $8 < V < 10$ m/s is about 3.3%. In this speed range the power loss does not vary significantly because the tip speed ratio (TSR) is constant and, therefore, the mean power coefficient C_P also remains constant. Below 5 m/s, the power loss is greater, due to lower TSR at low wind speed. From 10 to about 14 m/s, the power loss decreases from about 2% to 0, due to the compensation of the blade pitch control. At offshore TI level (right plot of Fig. 13) the trend of the power loss curves is similar to that at onshore TI level. The main difference is a faster power loss recovery as the rated power is approached, since the power loss vanishes for $V \geq 12$ m/s. This effect of the TI level on the curve of power loss was also observed and studied in Campobasso et al. (2023). The mean power loss level of most predictions for $8 < V < 10$ m/s is slightly lower than about 3.3%.

The AEP losses computed with the onshore power data reported in the left plot of Fig. 13 are presented in the left plot of Fig. 14. The adopted parameters of the Weibull PDF are those reported in the last row of Tab. 1. As expected on the basis of the onshore power data of Fig. 13, the use of both measured and computed force coefficients leads to a fairly constant AEP loss, amounting to about 2% in all cases. Also for the offshore conditions, consistently with the power data of Fig. 13 a fairly

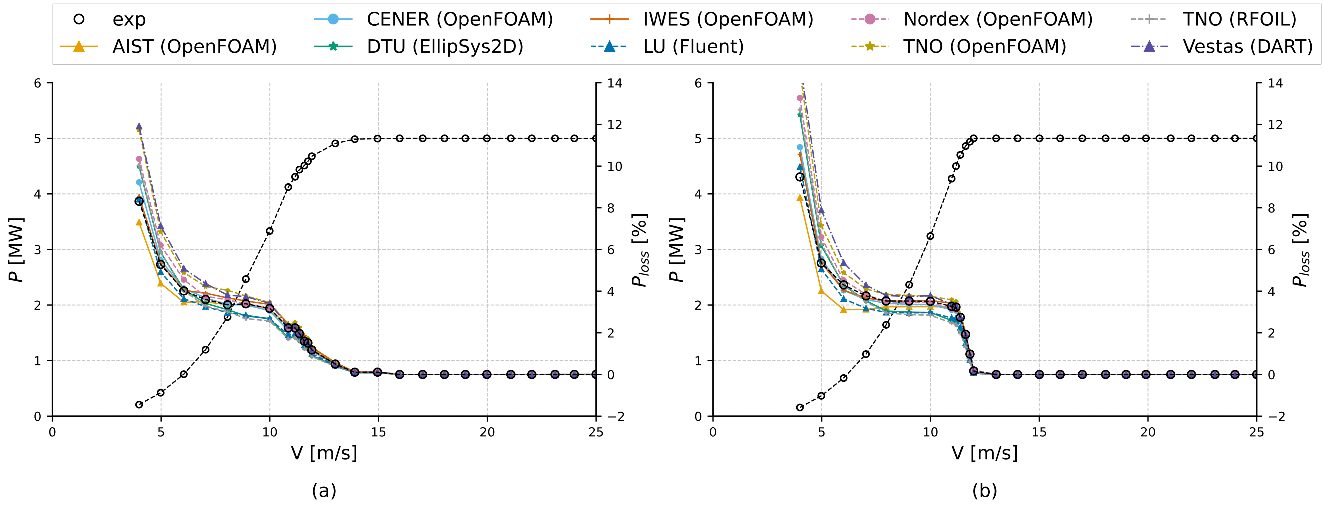

Figure 13. Power curve of NREL 5 MW WT obtained with measured force coefficients of nominal NACA 63_3-418 airfoil (read on left axis) and power loss curves obtained with measured and computed force coefficients of same airfoil without and with moderate LE degradation (read on right axis). All results refer to Texas A&M experiment. Left and right subplots refer to onshore and offshore TI levels, respectively.

constant AEP loss is obtained, amounting to about 1.4% using measured and computed aerodynamic data, with the parameters of the Weibull PDF being those reported in the first row of Tab. 1. 670

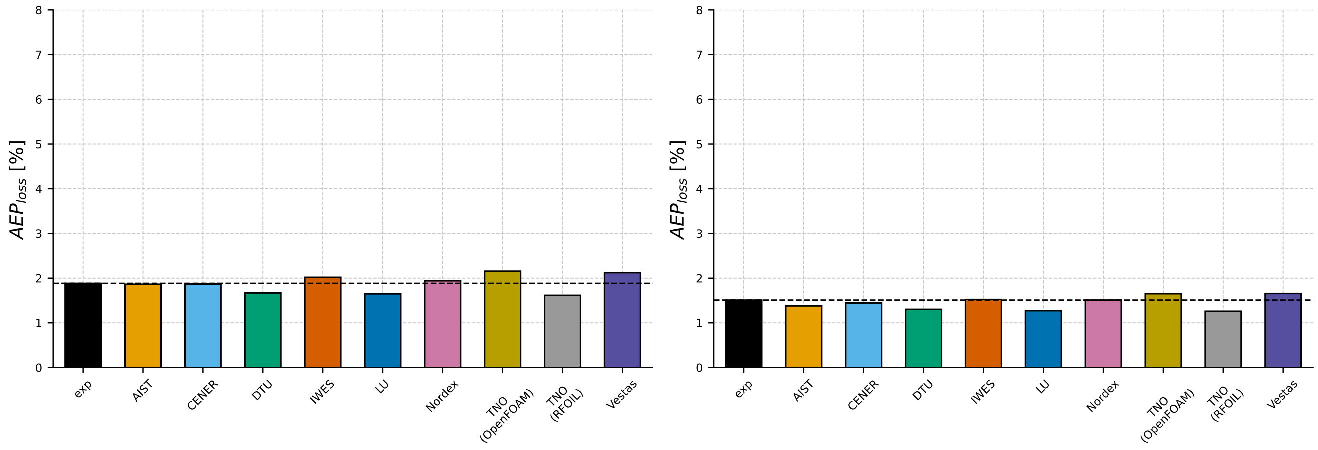

Figure 14. AEP loss of NREL 5 MW WT obtained with power data of Fig. 13 (Texas A&M experiment, NACA 63_3-418 airfoil affected by moderate LE degradation). Left and right subplots refer to onshore and offshore TI levels, respectively.

The mean value of the AoA over the outermost 30% of the blade length is about 5° for both the WT with the nominal blade and that with moderate LE degradation. The fact that the power loss curves of Fig. 13 and the AEP losses of Fig. 14 are fairly independent of the numerical method used to estimate the performance degradation of the NACA 63_3-418 airfoil may appear contradicting the significant spread of the c_l variations observed in the left plot of Fig. 5. That figure shows a c_l reduction varying between 0 (Vestas (DART)) and about 0.1 (AIST (OpenFOAM)). In order to investigate this aspect, the reductions of c_l, the increases of c_d and the reductions of c_l/c_d of the NACA 63_3-418 airfoil at $\alpha = 5°$, determined by using the wind tunnel measurements and all aerodynamic codes, are reported as percentages, respectively, in the left, middle and right plots of Fig. 15. In most cases, the mean level of the c_d increase of about 50% is about 10 times larger than the mean level of the c_l decrease of about 5%. Therefore, the AEP loss is dominated by the c_d increase due to moderate LE degradation, and this increase is, in most cases, fairly independent of the aerodynamic code used, and is also close to the measured value of 53.3%. The weight of the c_d increase on the AEP loss is emphasized by the results of the Vestas and TNO (OpenFOAM) predictions. In the former case, the predicted c_l reduction is 0 and in the latter it amounts to about 4.8%. The c_d increases predicted by the Vestas (DART) and TNO (OpenFOAM) analyses are 76% and 73.9%, respectively. Despite the notable difference in c_l drop, the onshore AEP loss corresponding to the two analyses is comparable and equal to about 2.1%. The lower weight of the c_l reduction on the AEP loss is also highlighted by the AIST (OpenFOAM) prediction. Despite this simulation yielding the largest c_l reduction of 10.4%, the corresponding AEP loss is close to those predicted by all other analyses. The low sensitivity of the AEP loss to the c_l reduction with moderate LE degradation is partly due to the fact that these reductions are notably smaller than the c_d increases. Moreover, the standard WT control reduces the rotational speed of the rotor with degraded LE (Collin et al.). The resulting AoA increase tends to increase c_l, partly compensating the c_l loss due to LE degradation, but it also further increases c_d. The relative weight of the c_l reduction and c_d increase of the degraded airfoil on the WT power reduction would be different using *adaptive control*, whereby the control uses the optimal TSR of the WT with degraded blade LE (Campobasso et al., 2020). A higher TSR of the degraded blades may result in the rotational speed increasing more rapidly with wind speed than for the rotor with clean blades and, consequently, different AoA variations.

Figure 16 analyzes the variations of the power curve due to the advanced LE degradation state of the NACA 63_3-418 airfoil considered in the Delft experiment. Similarly to Fig. 13, also Fig. 16 reports, for onshore TI on the left and offshore TI on the right, the power curve of the modified reference WT based on the measured force coefficients of the clean airfoil, the curve of the percentage power loss based on the measured force coefficients of the nominal and degraded airfoil, and the power loss curves obtained with the simulation codes presented in Section 3, except for the TNO (RFOIL) analysis.

The data of the left plot of Fig. 16 (onshore TI) show power losses notably larger than those observed with moderate LE degradation. Taking $V = 8$ m/s as a reference speed, the power loss based on the measured force coefficients is 11.4%. A larger scatter of the predicted power losses based on the airfoil performance predictions of all computer codes is also noted, with the loss at the reference speed varying between 6.9% (CENER (OpenFOAM)) and 12.6% (DTU (EllipSys2D)). At the reference speed, the power loss estimates based on computational aerodynamics closest to the measurement-based estimate are those of between 10.9% and 11.0% of the Nordex (OpenFOAM) and AIST (OpenFOAM) set-ups. At offshore TI level, the trend of the power loss curves is similar to that at onshore TI level, but power losses are slightly lower than in the latter condition.

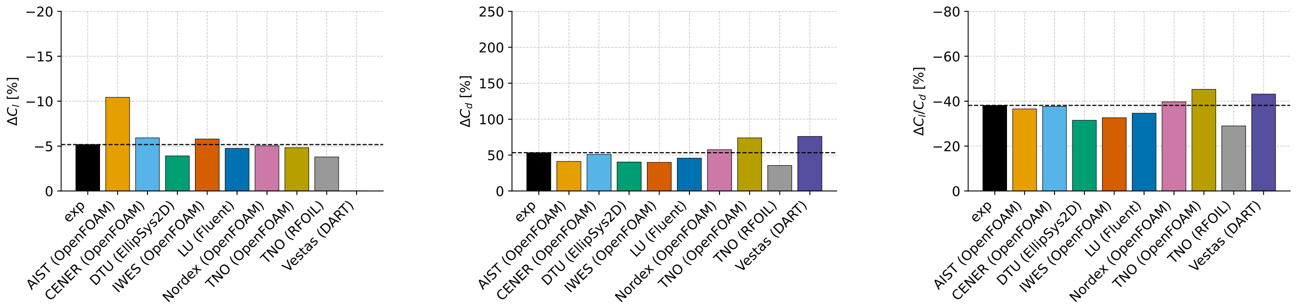

(a)

(b)

(c)

Figure 15. Comparison of measured and computed aerodynamic performance difference of clean and rough NACA 63_3-418 airfoils of the Texas A&M experiment at AoA $\alpha = 5°$: (a) lift coefficient percentage difference Δc_l; (b) drag coefficient percentage difference Δc_d; (c) percentage difference $\Delta(c_l/c_d)$.

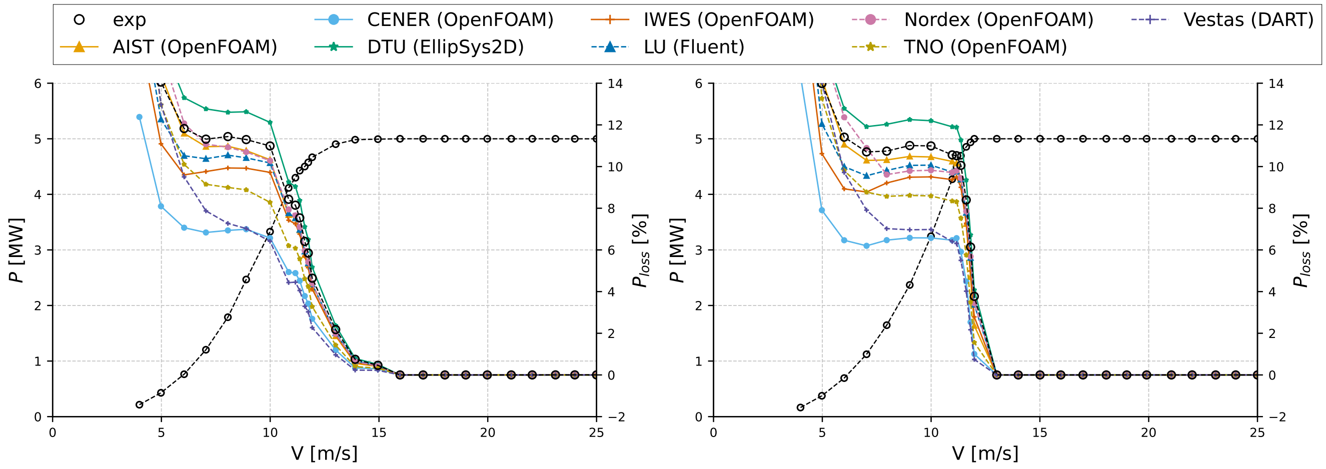

(a)

(b)

Figure 16. Power curve of NREL 5 MW WT obtained with measured force coefficients of nominal NACA 63_3-418 airfoil (read on left axis) and power loss curves obtained with measured and computed force coefficients of same airfoil without and with advanced LE degradation (read on right axis). All results refer to Delft experiment. Left and right subplots refer to onshore and offshore TI levels, respectively.

The power loss based on the measured force coefficients is 10.7%, and the other predictions vary between 6.5% and 12.0%. As in the case of moderate LE degradation, the main difference between the offshore and onshore cases is a faster power loss recovery as rated power is approached in the offshore case: the power loss vanishes for $V \geq 13$ m/s at offshore TI level, and for $V \geq 16$ m/s at onshore TI level.

The onshore AEP losses computed with the power data in the left plot of Fig. 16 are plotted in the left plot of Fig. 17. Unlike the case of moderate LE degradation, a significant variability of the predicted AEP losses based on the numerical estimates of the airfoil performance degradation is observed, consistently with the significant variability of the power loss curves in the left plot of Fig. 16. At onshore TI level, the AEP loss corresponding to the measured force coefficients is about 6.4%, and the closest aerodynamic simulation-based estimates of about 6.2% and 6.1% are obtained, respectively, by the Nordex (OpenFOAM) and AIST (OpenFOAM) analyses. The minimum AEP estimate of about 3.9% and the maximum AEP loss estimate of about 7.2% are obtained by the CENER (OpenFOAM) and the DTU (EllipSys2D) analyses, respectively. At offshore TI level, all AEP losses are lower than at onshore TI level: the measurement-based loss is about 4.9% and the closest aerodynamic simulation-based estimate are about 4.6% and 4.5%; the minimum and maximum AEP loss estimates are about 2.8% and 5.5%, respectively. The larger variability of the predicted AEP loss due to advanced LE degradation over that due to moderate degradation is due to larger variability of the predicted c_l decrease and c_d increase predictions in the case of the former degradation level.

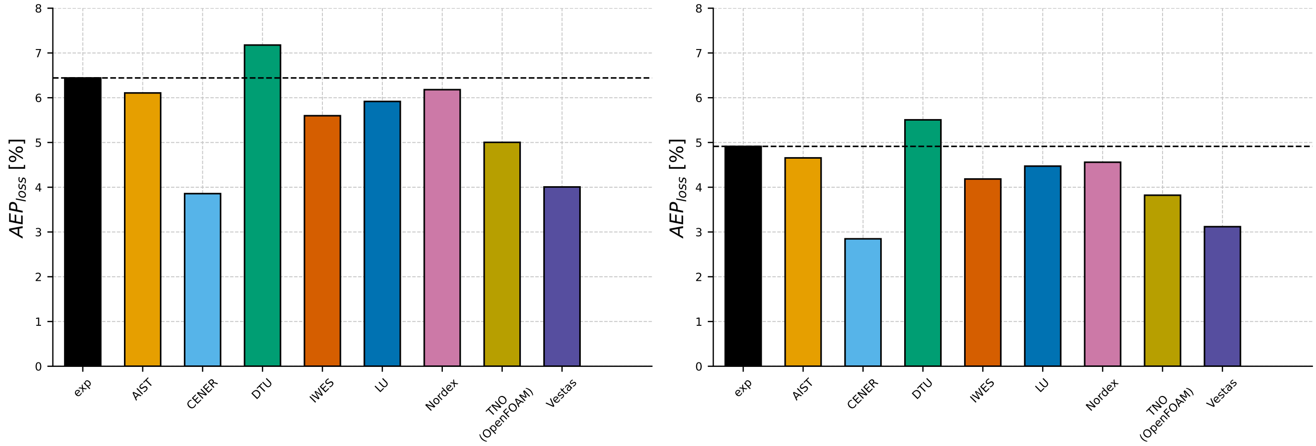

Figure 17. AEP loss of NREL 5 MW WT obtained with power data of Fig. 16 (Delft experiment, NACA 63_3-418 airfoil affected by advanced LE degradation). Left and right subplots refer to onshore and offshore TI levels, respectively.

In order to investigate in further detail the reasons for the fairly large variability of the estimated power and AEP losses associated with severe LE degradation, the percentage variations of cl, c_d and c_l/c_d based on the wind tunnel data and all computed results at the reference AoA $\alpha = 5°$ are examined in Fig. 18. Firstly, it is noted that the values of all three performance loss metrics are about twice as large with respect to those for the case of moderate LE degradation in Fig. 15. Furthermore, similarly to the case of moderate LE degradation, the mean level of the c_d increase is about 10 times larger than the mean level of the c_l decrease. Taking as a reference the measured force coefficients, it is found that severe LE degradation yields a c_d increase of about 160% and a c_l reduction of about 16%. Therefore, the weight of the drag increase is still likely to be larger than that of the lift reduction. This is also indicated by the fact that the pattern of the percentage c_d variations seen in the middle plot of Fig. 18 is fairly similar to that of the AEP losses in Fig. 17. However, the drag reduction predicted by the numerical methods depends much more on the computational set-up than found in the case of moderate LE degradation. This is the main cause of the larger variability of the predicted AEP loss. In turn, this larger variability is due to the fact that severe LE degradation brings also the outboard blade sections closer to stall-induced separations, a challenging phenomenon for RANS CFD predictions, which become more uncertain and sensitive to small variations of the adopted modeling methods and parameter choices. It is also observed that the overall pattern of the lift and drag variations in Fig. 18 are relatively similar, except for the Vestas (DART) case, because this method uses a lower-fidelity aerodynamic model. This qualitative correlation of drag and lift variations is an indication of the onset of stall-induced separation at the TE causing both a lift reduction and an increase of the profile loss.

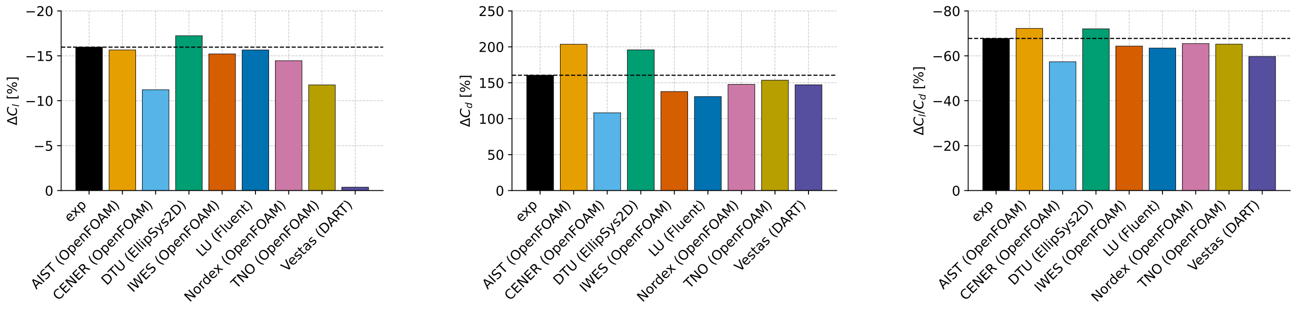

(a) (b) (c)

Figure 18. Comparison of measured and computed aerodynamic performance difference of clean and rough NACA 63_3-418 airfoils of the Delft experiment at AoA $\alpha = 5^\circ$: (a) lift coefficient percentage difference Δc_l; (b) drag coefficient percentage difference Δc_d; (c) percentage difference $\Delta(c_l/c_d)$.

6 Conclusions

This study has presented the main results of the First Aerodynamic Benchmark of IEA Wind Task 46 – Erosion of Wind Turbine Blades. The predictive capabilities of seven RANS CFD codes (ANSYS Fluent, EllipSys2D and five independent OpenFOAM set-ups) and two lower-fidelity methods (RFOIL and DART) have been cross-compared by considering measured force coefficients and transition location obtained from two separate wind tunnel testing campaign of a common wind turbine airfoil. The measured data referred to the NACA 63_3-418 airfoil tested with clean and moderately degraded LE in the Texas A&M wind tunnel, and with clean and severely degraded LE in the Delft wind tunnel. The analysis of the measured data indicates that LE degradation decreases lift and increases drag before stall at both LE degradation levels considered. Above stall, however, the low-level roughness associated with moderate LE degradation appears to reduce the severity of stall and

https://doi.org/10.5194/wes-2026-89
Preprint. Discussion started: 3 June 2026

the performance reduction. Conversely, the severe level of LE degradation exacerbates the post-stall lift reduction and drag increase, as expected.

At moderate LE degradation, most codes predict fairly well the measure airfoil force coefficient for both the clean and degraded LE before stall. Then, they tend to overestimate the aerodynamic performance of the airfoil in the stall and post-stall region, but the predictions of most codes in this AoA range are closer to the measured force coefficients for the rough LE case than for the clean LE case. Overall, the codes predict a drag increase due to LE roughness fairly close to the measurement-based values in the AoA range typical of the design operating conditions of the outboard blade of utility-scale WTs. It is also noted that the percentage drag increase due to LE degradation is about 10 times larger than the percentage lift reduction. The cross-comparison of the predictions of the SS BL transition for the clean LE case appear to show slightly better performance of the e^N method over the $\gamma - Re_\theta$ SST model.

At severe LE degradation, most computational aerodynamics codes predict reasonably well the measure airfoil force coefficient for both the clean and degraded LE. However, although the measured and computed c_l curves are parallel to each other, there is a slightly larger offset among them, most likely due to the lack of the actual geometry used in the wind tunnel and consequent possible small differences in the airfoil geometry used by the participants. Each participant, however, used the same airfoil geometry for the clean and degraded LE geometry, which gives confidence in the predicted performance degradation being fairly independent of small differences in the airfoil geometry. All codes overestimate the aerodynamic performance of the airfoil in the stall and post-stall region, but, similarly to the moderate LE degradation case, the predictions in this AoA range are closer to the measurements for the rough LE case than for the clean LE case. Overall, the codes predict a drag coefficient of the clean airfoil fairly close to the measured values in the AoA range typical of the design operating conditions of the outboard blade of utility-scale WTs, but with significant variations. In the case of degraded LE, although the values of the predicted c_d averaged among all predictions are close to the measured values, the individual predicted values differ considerably more among themselves than they do in the case of moderate LE degradation. Consequently, a significant variation in the predicted performance loss is observed. This is caused by the modeling challenges associated with analyzing the effects of severe LE degradation and the impact of different roughness modeling choices. Also with severe LE degradation, the percentage drag increase due to LE degradation is about 10 times larger than the percentage lift reduction, but the average lift and drag variations are three times larger than with moderate degradation.

In order to estimate the AEP loss due to the considered LE degradation states, the NREL 5 MW operating at typical onshore and offshore sites has been considered. In the case of moderate LE degradation, the AEP loss at onshore and offshore site is found to be about 2% and 1.5%, respectively, with very little variations among predictions. This is a consequence of the small variations of c_d increase among predictions and a relatively small dependence on the c_l reduction at the typical operating AoA of the outboard blade. Conversely, in the case of severe LE degradation a significant variability of the predicted AEP loss is observed. At the considered onshore conditions, the AEP loss predicted on the basis of the measured force coefficients is about 6.4%, whereas the minimum and maximum loss estimates based on the computer-based airfoil analyses are 3.9% and 7.2%, respectively. The offshore AEP loss based on the measured force coefficients is about 4.9%, whereas the minimum and maximum loss estimates based on the computer-based airfoil analyses are 2.9% and 5.5%, respectively. This is a consequence of the large variability in the predicted drag increase.

The results of the benchmark highlight the necessity of improving the methods to determine the impact of advanced LE degradation on airfoil performance degradation. These improvements range from developing more sophisticated distributed roughness models or even resolving the geometry of LE eroded by atmospheric precipitation or contaminated by dust and insect accumulation to using higher-fidelity methods for resolving turbulence, such as Large Eddy Simulations (LES) or hybrid RANS/LES methods.

Data availability. The experimental data of the Texas A&M wind tunnel experiment are available at https://wdh.energy.gov/ds/lees/report.z01.00; the experimental data of the Delft wind tunnel experiment are available at https://zenodo.org/records/3482801#.YpcDL-7P3IU; all simulation data are available upon request.

Appendix A: Numerical and physical parameters of CFD simulations

All codes use the k-ω SST model for the turbulence closure, with the value of the constant a_1 provided in the third column of Tab. A1. The second column of the table indicates the adopted CFD code, with the abbreviation "OF" standing for OpenFOAM. Codes featuring methods to preserve the ambient turbulence between the inflow boundary and the airfoil used a TI value very close to that of the experiments; the other codes used a suitable combination of increased TI and value of ω, the second turbulent variable of the k-ω SST model, to achieve a TI value close to the measured value at the airfoil LE. The codes using the ambient TI of the experiments are indicated in the last column of Tab. A1.

Table A1. Overview of CFD solvers and simulation setups.

Org.	Solver	a_1	Transition	Roughness	Ambient turb.
AIST	OF v2106	0.31	γ-Re_θ	Cebeci-Bradshaw	
CENER	OF v2306	0.28	γ-Re_θ	Wilcox + Hellsten	✓
DTU	EllipSys2D v24	0.31	e^N	Knopp	✓
IWES	OF v2306	0.29	γ-Re_θ	Cebeci-Bradshaw	
LU	Fluent v21R	0.29	γ-Re_θ	Cebeci-Bradshaw	
Nordex	OF v9	0.31	γ-Re_θ	Wilcox + Hellsten	
TNO	OF v2012	0.31	γ-Re_θ	Dassler + Wilcox	

Org.: Organisation; ✓: Active

The main parameters of the grids used by all CFD codes for the simulation of the Texas A&M and Delft experiments are reported in Tables A2 and A3, respectively. The second, third and fourth columns report, respectively, the structured grid topology, the total number of cells and the number of cells on the airfoil surface. The fifth column, labeled "FF" provides the distance of the far-field boundary from the airfoil in terms of number of chords. The sixth column gives the cell height of the wall-adjacent cells δ_w normalized by the chord. All CFD analyses, except that of IWES, use the same grid for simulating the flow field past a given airfoil without and with roughness. The IWES set-up uses a different grid for the clean and rough LE cases. More specifically, the grids for the clean and airfoil analyses differ only by the minimum wall distance δ_w. Tables A2 and A3 provide the value of this parameter used for both analysis types, with the figure followed by "C" in the clean analysis case and "(R)" in the rough analysis case. For most CFD analyses, the last column of the two tables also reports the value of the equivalent sand-grain roughness K_s, normalized by c, used in the rough airfoil simulations. In the case of the TNO analyses. the last column of the tables give the engineering roughness K, and not K_s. This is because TNO uses an in-house numerical model to determine the value of K_s used in the simulations, using the value of K and the roughness density as input of the in-house numerical tool.

Table A2. Overview of grid and roughness parameters for simulations of NACA 63_3-418 airfoil of Texas A&M experiment at Re=3.2M.

Org.	Topol.	Tot. cells	Surf. cells	FF [c]	$\delta_w/c \times 10^6$	$K_s/c \times 10^6$
AIST	H	260065	638	40	250	101
CENER	O	124251	499	80	0.425	200
DTU	O	131072	512	45	0.1	101
IWES	O	131072	512	300	2.1 (C) / 168 (R)	200
LU	C	110852	530	50	7.7	101
Nordex	O	135405	531	40	1.1	101
TNO	O	209792	704	90	0.8	246*

*: indicates chord-scaled technical roughness K, not K_S.

Table A3. Overview of grid and roughness parameters for simulations of NACA 63_3-418 airfoil of Delft experiment at Re=3.0M.

Org.	Topol.	Tot. cells	Surf. cells	FF [c]	$\delta_w/c \times 10^6$	$K_s/c \times 10^6$
AIST	H	259734	734	40	250	5000
CENER	O	124251	499	80	0.425	1000
DTU	O	131072	512	45	0.1	5000
IWES	O	131072	512	316	2.1 (C) / 168 (R)	708
LU	C	120486	596	50	7.0	5000
Nordex	O	135405	531	40	1.1	5000
TNO	O	209792	704	90	6	708*

*: indicates chord-scaled technical roughness K, not K_S.

Author contributions. MSC led the preparation of the manuscript and the revision of all presented analyses. AC performed the turbine power and AEP analyses, supported the LU CFD analyses and contributed to the analysis of all results. DB carried out all CENER CFD analyses, postprocessed all measured data and numerical results and designed and implemented their graphical comparison. BM and DCM contributed to all reported analyses. JNT performed all IWES CFD analyses. AMF performed all DTU CFD analyses with code support by NNS. KV

and MC performed all CFD and RFOIL TNO analyses. RG and YG performed all NORDEX CFD analyses. AA performed all AIST CFD analyses, and FG performed all Vestas DART analyses.

Competing interests. The authors have no competing interests to declare.

Disclaimer. Fraunhofer IWES and CENER: views and opinions expressed are those of the author(s) only and do not necessarily reflect those of the European Union. Neither the European Union nor the granting authority can be held responsible for them.
Sandia National Laboratories: this article describes objective technical results and analysis. Any subjective views or opinions that might be expressed in the article do not necessarily represent the views of the U.S. Department of Energy or the United States Government.

Acknowledgements. Lancaster University (LU): this work was supported by the UK Engineering and Physical Sciences Research Council, Grant EP/W524438/1. The simulations were performed on LU's HEC cluster.
Sapienza University of Rome: this work was supported by the Italian ”Ministero dell'Ambiente e della Sicurezza Energetica” through Grant ”RdS PTR 2025-2027 - Energia dal mare”.
Fraunhofer IWES: this work was carried out as part of the AIRE project, funded under the EU Programme Horizon Europe, grant Agreement 101083716. The simulations were partly performed on the HPC Cluster MOUSE at the University of Oldenburg (Germany) funded by BMWK (grant number 03EE3067 B).
Sandia National Laboratories is a multimission laboratory managed and operated by National Technology & Engineering Solutions of Sandia, LLC, a wholly owned subsidiary of Honeywell International Inc., for the U.S. Department of Energy's National Nuclear Security Administration under contract DE-NA0003525.
AIST: this work was supported by the project of Fukushima prefecture "Establishment of a Hub for Technology and Human Resource Development on Improved Operation and Maintenance of Wind Power Generation". The numerical analyses were performed using the FUJITSU Supercomputer PRIMEHPC FX1000 and FUJITSU Server PRIMERGY GX2570 (Wisteria/BDEC-01) at the Information Technology Center, The University of Tokyo.
CENER: this work has been supported by the AIRE project funded under the EU Programme Horizon Europe. Grant Agreement 101083716.
DTU Wind's efforts were supported by the LERCat project (Danish Energy Council: EUDP-64021-2027), the AIRE project (EU: HORIZON-CL5-2021-D3-03, No. 101083716) and IEA Task 46 (Danish Energy Council: EUDP-134243-532862).
All authors of this article are members of the Aerodynamics Working Group of IEA Wind Task 46, who designed and performed the study reported herein.

References

Abbott, I. and Von Doenhoff, A.: Theory of Wing Sections, Including a Summary of Airfoil Data, Dover Books on Aeronautical Engineering Series, Dover Publications, ISBN 9780486605869, https://books.google.co.uk/books?id=DPZYUGNyuboC, 1959.

Adeel-Ur-Rehman, A., Theron, J., Kassem, H., Stoevesandt, B., and Peinke, J.: Improved performance of k - ω SST turbulence model in predicting airfoil characteristics for a wide range of airfoil thicknesses, Journal of Physics: Conference Series, 2767, 022 064, 2024.

Barber, S., Wang, Y., Jafari, S., Chokani, N., and Abhari, R. S.: The Impact of Ice Formation on Wind Turbine Performance and Aerodynamics, Journal of Solar Energy Engineering, 133, 011 007, https://doi.org/10.1115/1.4003187, 2011.

Bardal, L. M. and Sætran, L. R.: Influence of turbulence intensity on wind turbine power curves, Energy Procedia, 137, 553–558, 2017.

Bech, J., Hasager, C., and Bak, C.: Extending the life of wind turbine blade leading edges by reducing the tip speed during extreme precipitation events, Wind Energy Science, 3, 729–748, 2018.

Berge, E., Byrkjedal, Ø., Ydersbond, Y. W., and Kindler, D.: Modelling of offshore wind resources. Comparison of a mesoscale model and measurements from FINO 1 and North Sea oil rigs, european Wind Energy Conference, Marseille, France, 2009.

Caccia, F. and Guardone, A.: Numerical simulations of ice accretion on wind turbine blades: are performance losses due to ice shape or surface roughness?, Wind Energy Science, 8, 341–362, https://doi.org/10.5194/wes-8-341-2023, 2023.

Campobasso, M., Cavazzini, A., and Minisci, E.: Rapid Estimate of Wind Turbine Energy Loss due to Blade Leading Edge Delamination Using Artificial Neural Networks, Journal of Turbomachinery, 142, https://doi.org/10.1115/1.4047186, 2020.

Campobasso, M., Castorrini, A., Cappugi, L., and Bonfiglioli, A.: Experimentally validated three-dimensional computational aerodynamics of wind turbine blade sections featuring leading edge erosion cavities, Wind Energy, 25, 168–189, 2022.

Campobasso, M. S., Castorrini, A., Ortolani, A., and Minisci, E.: Probabilistic analysis of wind turbine performance degradation due to blade erosion accounting for uncertainty of damage geometry, Renewable and Sustainable Energy Reviews, 178, 113 254, 2023.

Campobasso, M. S., Rose, M. S., Shende, S., Adirosi, E., Pace, G., De Silvestri, L., Dimitriadou, K., Vinod, A., Hassager, C. B., Sánchez, F., and Castorrini, A.: Development, performance and energy trade-off analyses of wind turbine precipitation-reactive control at offshore and onshore sites in Western Europe, Renewable Energy, 262, 125 357, https://doi.org/https://doi.org/10.1016/j.renene.2026.125357, 2026.

Cappugi, L., Castorrini, A., Bonfiglioli, A., Minisci, E., and Campobasso, M.: Machine learning-enabled prediction of wind turbine energy yield losses due to general blade leading edge erosion, Energy Conversion and Management, 245, 114 567, 2021.

Castorrini, A., Ortolani, A., and Campobasso, M. S.: Assessing the progression of wind turbine energy yield losses due to blade erosion by resolving damage geometries from lab tests and field observations, Renewable Energy, 218, 119 256, https://doi.org/https://doi.org/10.1016/j.renene.2023.119256, 2023.

Cebeci, T. and Bradshaw, P.: Momentum Transfer in Boundary Layers, Hemisphere Publishing Corporation, New York, 1977.

Collin, T., Castorrini, A., Shende, S., Meyer Forsting, A., and Campobasso, M.: Can vortex generators reduce power losses of utility-scale wind turbines due to blade leading edge erosion?, Journal of Physics: Conference Series, Accepted.

Drela, M.: XFOIL: An Analysis and Design System for Low Reynolds Number Airfoils, in: Low Reynolds Number Aerodynamics, vol. 54 of *Lecture Notes in Engineering*, Springer Verlag, 1989.

Drela, M. and Giles, M. B.: Viscous-inviscid analysis of transonic and low Reynolds number airfoils, AIAA Journal, 25, 1347–1355, https://doi.org/10.2514/3.9789, 1987.

Ehrman, E.: Degradation of Wind-Turbine Blade Performance due to Roughness Contamination, Ph.D. thesis, Texas A&M University, Texas, USA, 2014.

Ehrmann, R. and White, E.: Influence of 2D Steps and Distributed Roughness on Transition on a NACA 63(3)-418, AIAA paper 2014-0170, 32nd ASME Wind Energy Symposium, National Harbor, Maryland, 2014.

Ehrmann, R. S., Wilcox, B., White, E. B., and Maniaci, D. C.: Effect of Surface Roughness on Wind Turbine Performance, Sandia Report SAND2017-10669, Sandia National Laboratories, Albuquerque, NM, https://www.sandia.gov/app/uploads/sites/273/2025/02/LEE_Ehrmann_SAND2017-10669.pdf, 2017.

Emeis, S.: Current issues in wind energy meteorology, Meteorological Applications, 21, 803–819, 2014.

Guan, X., Zong, L., Liu, B., and Kong, D.: Research on Erosion Wear of Wind Turbine Blades by Sand-Carrying Wind Based on EDEM, Applied Solar Energy, 61, 47–57, https://doi.org/10.3103/S0003701X24600036, 2025.

Gutiérrez, R., Aranguren, P., and Zamponi, R.: Improved RANS methodology to account for flow separation on rough blades, Journal of Physics: Conference Series, 2767, 022 002, 2024.

Han, W., Kim, J., and Kim, B.: Effects of contamination and erosion at the leading edge of blade tip airfoils on the annual energy production of wind turbines, Renewable Energy, 115, 817–823, 2018.

Hellsten, A. and Laine, S.: Extension of the $k-\omega$ Turbulence Model for Flows over Rough Surfaces, AIAA paper 97-3577, 22nd Atmospheric Flight Mechanics Conference, New Orleans, LA, 1997.

Herring, R., Dyer, K., Martin, F., and Ward, C.: The increasing importance of leading edge erosion and a review of existing protection solutions, Renewable and Sustainable Energy Reviews, 115, 109 382, 2019.

IEA Wind TCP: Task 46 – Erosion of Wind Turbine Blades, https://iea-wind.org/task46/, accessed on 10 May 2026.

Im, H. and Kim., B.: Numerical study on the effect of blade surface deterioration by erosion on the performance of a large wind turbine, Journal of Renewable and Sustainable Energy, 11, 063 308, 2019.

Jin, J. Y., Karlsson, T., and Virk, M. S.: Wind Turbine Ice Detection Using AEP Loss Method – A Case Study, Wind Energy Science Discussions, 2021, 1–14, https://doi.org/10.5194/wes-2021-55, 2021.

Jonkman, B. and Kilcher, L.: TurbSim: A stochastic, full-field, turbulence simulator primarily for use with InflowWind/AeroDyn-based simulation tools., https://www.nlr.gov/wind/nwtc/turbsim, national Laboratiry of the Rockies, Golden, Colorado. Accessed on 30 April 2026.

Jonkman, J. and Sprague, M.: OpenFAST: An aeroelastic computer-aided engineering tool for horizontal axis wind turbines, https://www.nlr.gov/wind/nwtc/openfast, national Laboratiry of the Rockies, Golden, Colorado. Accessed on 30 April 2026.

Jonkman, J., Butterfield, S., Musial, W., and Scott, G.: Definition of a 5-MW Reference Wind Turbine for Offshore System Development, Tech. Rep. NREL/TP-500-38060, NREL, Golden, CO, USA, 2009.

Kato, M. and Launder, B.: The modelling of turbulent flow around stationary and vibrating square cylinders, paper 10-4, 9th Symposium on Turbulent Shear Flows, Kyoto, Japan, 1993.

Keegan, M. H., Nash, D. H., and Stack, M. M.: On erosion issues associated with the leading edge of wind turbine blades, Journal of Physics D: Applied Physics, 46, 383 001, https://doi.org/10.1088/0022-3727/46/38/383001, 2013.

Knopp, T., Eisfeld, B., and Bartolome Calvo, J.: A new extension for k–ω turbulence models to account for wall roughness, International Journal of Heat and Fluid Flow, 30, 54–65, https://doi.org/10.1016/j.ijheatfluidflow.2008.09.009, 2009.

Kolmogorov, D. K., Shen, W. Z., Sørensen, N. N., and Sørensen, J. N.: Fully consistent SIMPLE-like algorithms on collocated grids, Numerical Heat Transfer, Part B: Fundamentals, 67, 101–123, 2015.

Koodly Ravishankara, A., Özdemir, H., and van der Weide, E.: Analysis of leading edge erosion effects on turbulent flow over airfoils, Renewable Energy, 172, 765–779, 2021.

Kruse, E., Bak, C., and Olsen, A.: Wind tunnel experiments on a NACA 63_3-418 airfoil with different types of leading edge roughness, Wind Energy, https://doi.org/10.1002/we.2630, 2021.

Langel, C., Chow, R., Hurley, O., Van Dam, C., Maniaci, D., Ehrmann, R., and White, E.: Analysis of the Impact of Leading Edge Surface Degradation on Wind Turbine Performance, AIAA paper 2015-0489, 33rd ASME Wind Energy Symposium, Kissimmee, Florida, 2015.

Langel, C., Chow, M., Van Dam, C., and Maniaci, D.: RANS Based Methodology for Predicting the Influence of Leading Edge Erosion on Airfoil Performance, Tech. Rep. SAND2017-11289, Langley Aeronautical Laboratory, Albuquerque, New Mexico and Livermore, California, 2017.

Langtry, R. and Menter, F.: Correlation-Based Transition Modeling for Unstructured Parallelized Computational Fluid Dynamics Codes, AIAA Journal, 47, 2894–2906, 2009.

Langtry, R., Menter, F., , Likki, S., Suzen, Y., Huang, P., and Völker, S.: A Correlation-Based Transition Model Using Local Variables — Part II: Test Cases and Industrial Applications, Journal of Turbomachinery, 128, 423–434, 2006.

Leonard, B.: A stable and accurate convective modelling procedure based on quadratic upstream interpolation, Computer Methods in Applied Mechanics and Engineering, 19, 59–98, 1979.

Lopez, J. C., Kolios, A., Wang, L., Chiachio, M., and Dimitrov, N.: Reliability-based leading edge erosion maintenance strategy selection framework, Applied Energy, 358, 122 612, https://doi.org/https://doi.org/10.1016/j.apenergy.2023.122612, 2024.

Mack, L. M.: Transition and laminar instability, Tech. Rep. JPL-PUBL-77-15, 1977.

Maniaci, D. and White, E.: Leading-edge Erosion Study (LEES) Project: Owner Reports-Airfoil Performance Degradation due to Roughness and Leading-edge Erosion, data and plots-Raw Data, Tech. rep., Wind Data Hub operated and maintained by Pacific Northwest National Lab.(PNNL) at https://wdh.energy.gov, https://doi.org/10.21947/1373097, 2020.

Maniaci, D., White, E., Wilcox, B., Langel, C., van Dam, C., and Paquette, J.: Experimental Measurement and CFD Model Development of Thick Wind Turbine Airfoils with Leading Edge Erosion, Journal of Physics: Conference Series, 753, 022 013, 2016.

Maniaci, D. C., Meyer Forsting, A., Barlas, A., Bak, C., and Olsen, A. S.: Model to Predict Annual Energy Production Loss Based on Blade Erosion Class, Technical Report WP3.1, IEA Wind TCP Task 46, 2025.

Menter, F.: Zonal Two Equation K-ω Turbulence Models for Aerodynamic Flows, AIAA paper 93-2906, 24th AIAA Fluid Dynamics Conference, Orlando, Florida, 1993.

Menter, F.: Two-Equation Turbulence-Models for Engineering Applications, AIAA Journal, 32, 1598–1605, 1994.

Menter, F. and Esch, T.: Elements of Industrial Heat Transfer Predictions, Technoical paper, 16th Brazilian Conference of Mechanical Engineering, Uberlândia, Minas Gerais, Brazil, 2001.

Menter, F., Kuntz, M., and Langtry, R.: Ten Years of Industrial Experience with the SST Turbulence Model, in: Turbulence, Heat and Mass Transfer 4, edited by K. Hanjalic, Y. Nagano, M. T. E., pp. 625–632, Bergell House Inc., 2003.

Menter, F., Langtry, R., Likki, S., Suzen, Y., Huang, P., and Völker, S.: A Correlation-Based Transition Model Using Local Variables — Part I: Model Formulation, Journal of Turbomachinery, 128, 413–422, 2006.

Michelsen, J. A.: Basis3D - a Platform for Development of Multiblock PDE Solvers, Tech. Rep. AFM 92-05, Technical University of Denmark, Department of Fluid Mechanics, Technical University of Denmark, 1992.

Michelsen, Jess A.: Forskning i aeroelasticitet (Research in aeroelasticity) EFP-2001, chap. 6. Beregning af laminar-turbulent omslag i 2D og 3D (Computation of laminar-turbulent transition in 2D and 3D), Risø-R-1349(DA), Forskningscenter Risø (now DTU Wind), ISBN 87-550-3078-5, 2002.

Mishnaevsky, L., Hasager, C. B., Bak, C., Tilg, A.-M., Bech, J. I., Doagou Rad, S., and Fæster, S.: Leading edge erosion of wind turbine blades: Understanding, prevention and protection, Renewable Energy, 169, 953–969, 2021.

Nikuradse, J.: Laws of flow in rough pipes, Technical Memorandum NASA TM 1292, Lewis Research Center, Washington, USA, 1950.

Ortolani, A., Castorrini, A., and Campobasso, M.: Multi-scale Navier-Stokes analysis of geometrically resolved erosion of wind turbine blade leading edges, Journal of Physics: Conference Series, 2265, 032 102, 2022.

Pires, O., Munduate, X., Boorsma, K., Yilmaz, O. C., Madsen, H. A., and Timmer, W.: Experimental investigation of Surface Roughness effects and Transition on Wind Turbine performance, Journal of Physics: Conference Series, 1037, 052 018, 2018.

Pryor, S. C. and Barthelmie, R. J.: Hail as a damage vector for renewable energy, iScience, 29, 114 439, https://doi.org/https://doi.org/10.1016/j.isci.2025.114439, 2026.

Schlichting, H.: Experimentelle Untersuchungen zum Rauhigkeitsproblem, Ingenieur - Archiv, 7, 1—34, english translation: 1937. Experimental investigation of the problem of surface roughness. NACA TM 823, 1936.

Schlichting, H.: Experimental Investigation of the Problem of Surface Roughness, Tech. Rep. Technical Memorandum 823, NACA, WA, USA, 1937.

Smith, A. and Gamberoni, N.: Transition, Pressure Gradient, and Stability Theory, Tech. Rep. Douglas Aircraft Rept. ES-26388, 1956.

Somers, D.M.: The S814 and S815 Airfoils, Tech. Rep. NREL/SR-500-36292, NREL, Golden, CO, USA, 2004.

Sørensen, N. N.: General purpose flow solver applied to flow over hills, 1995.

Spalart, P. R. and Rumsey, C. L.: Effective Inflow Conditions for Turbulence Models in Aerodynamic Calculations, AIAA Journal, 45, 2544–2553, 2007.

Timmer, W. A. and Schaffarczyk, A. P.: The effect of roughness at high Reynolds numbers on the performance of aerofoil DU 97-W-300Mod, Wind Energy, 7, 295–307, 2004.

van Ingen, J.: Suggested Semi-Empirical Method for the Calculation of the Boundary Layer Transition Region, Tech. Rep. Delft Univ. of Technology Rept. VTH-74, Dept. of Aerospace Engineering, 1956.

van Rooij, R. A.: Modification of the boundary layer calculation in RFOIL for improved airfoil stall prediction, Tech. Rep. IW-96087R, TU Delft, 1996.

Vimalakanthan, K., van der Mijle Meijer, H., Bakhmet, I., and Schepers, G.: Computational fluid dynamics (CFD) modeling of actual eroded wind turbine blades, Wind Energy Science, 8, 41–69, 2023.

Wang, J., Gao, J., Zhang, Y., and Cui, H.: Analysis of the Sand Erosion Effect and Wear Mechanism of Wind Turbine Blade Coating, Energies, 17, https://doi.org/10.3390/en17020413, 2024.

Wilcox, D.: Reassessment of the Scale-Determining Equation for Advanced Turbulence Models, AIAA Journal, 26, 1299–1310, 1988.

Wood, R. J. K. and Lu, P.: Leading edge topography of blades–a critical review, Surface topography: metrology and properties, 9, 023 001, 2021.

Zanon, A., De Gennaro, M., and Kuehnelt, H.: Wind energy harnessing of the NREL 5 MW reference wind turbine in icing conditions under different operational strategies, Renewable Energy, 115, 760–772, 2018.